# Stress distribution in depth of NiCr + Cr2O3 systems using high-energy synchrotron X-rays in transmission mode

Zhimao Wang, Jean-Luc Grosseau-Poussard, Guillaume Geandier, Benoît Panicaud

# Stress distribution in depth of NiCr + $Cr_2O_3$ systems using high-energy synchrotron X-rays in transmission mode

Zhimao Wang [1], Jean-Luc Grosseau-Poussard [2], Guillaume Geandier [3], Benoît Panicaud [1*]

[1] Université de Technologie de Troyes (UTT), Institut Charles Delaunay (ICD), Systèmes Mécaniques et d'Ingénierie Simultanée (LASMIS), 12 rue Marie Curie, CS 42060, 10004, Troyes Cedex, France;

[2] Laboratoire des Sciences de l'Ingénieur pour l'Environnement (LaSIE), Université de La Rochelle, CNRS UMR 7356, Avenue Michel Crépeau, 17042, La Rochelle Cedex 1, France;

[3] Institut Jean Lamour, CNRS UMR 7198, Université de Lorraine, Campus ARTEM, 2 Allée André Guinier, BP 50840, 54011 Nancy Cedex, France

* Correspondence: benoit.panicaud@utt.fr; Tel.: +333 25 71 80 61

Received: date; Accepted: date; Published: date

Abstract: NiCr alloys develop chromia layers in oxidizing high temperature environments. The stress in oxide layer was largely explored, whereas too few works were devoted to the stress distribution in the underlying metallic substrate. To determine the stress distribution in a duplex oxide-metallic substrate system, a variant of $\sin^2\psi$ method in transmission mode using high-energy synchrotron X-rays has been developed. 103.4 keV synchrotron X-rays have been used to penetrate 6x6x0.4 mm and Ø6x0.9 mm samples with different oxidation conditions. In order to obtain the stress gradient from the top surface to the bottom surface, the patterns of diffraction were collected and then were analyzed by a complete data processing. The stress varies towards the surface in a non-linear manner, especially near the interface zone. In order to better understand the stress distribution of such a duplex oxide-metallic substrate system, the stress caused by chromium diffusion is investigated by proposing numerical values for coupling coefficient, which finally can partially explain the stress variation near the interface zone.

Keywords: High-energy synchrotron X-rays; Transmission mode; Chromium diffusion; Stress distribution; Oxidation of chromium alloys; Chromium concentration profiles

## 1. Introduction

### 1.1. Background and Motivations

Usually, an oxide layer grows during the oxidation of a metal or metallic alloy in oxidizing high temperature environments. Chromium-based alloys form a chromia layer in these environments such as nuclear power plants, thermal power stations, gas turbines etc. During the formation of such an oxide layer, residual stress generally arises, because of incompatibilities between the oxide layer and the metallic substrate. Residual stress is a serious problem that can affect the mechanical balance of the structure and the integrity of the metal [1-3].

Regarding to the generation of residual stress, there are two main sources of stress in an oxide layer. One of these is due to growth stresses in the oxide layer, which can occur even during isothermal oxidation. The second type is thermal stress due to changes in temperature over time and is caused by a mismatch of the thermal expansion coefficients between the oxide layer and the metal substrate. These two kinds of stresses are widely reported in previous researches [4-6].

In contrast, the stress spatial distribution in the metallic substrate has been less studied. The main challenge of the measurement is that conventional X-ray diffraction (XRD) performed at laboratory

does not generally have sufficient energy to penetrate a large depth to obtain bulk information. Furthermore, from preliminary XRD tests did with conventional goniometer, in the reflexion mode, the stress obtained is an average over the penetrated depth (around 10 μm), so that the local stress distribution as a function of depth cannot be obtained with a constant wavelength. However, some previous works seem to evidence a non-uniform stress distribution in the substrate. For example, there are articles exploring the stress distribution using the curvature method [7, 8], which lead to a stress calculated as a function of depth.

To improve our understanding of the spatial stress distribution in the substrate for a duplex oxide-metallic substrate system, a variant of $\sin^2\psi$ method in transmission mode with high-energy synchrotron X-rays has been developed. Such kind of method was already used to determine residual stress in Thermal Barrier Coatings [9], which demonstrates the possibility to measure directly the stress as a function of depth.

### 1.2. Aims of the work

The present work seeks to further explore and understand the residual stress distribution in the metallic substrate after oxidation, especially how the stress spatially distributes in the substrate in relation to the oxide layers growth mechanisms. Knowing the distribution of residual stress will help us to prevent damage effect.

In the present work, the residual stresses as a function of depth in the metal are determined. To better understand the stress distribution in an oxide-metal system, the stress induced by chromium diffusion is particularly investigated. The corresponding set of questions aim to analyze the relation between chromium concentration profiles in the metal and the stress distribution in the near interface zone. With the addition of diffusion stresses to existing modelling, a better agreement between the theoretical stresses and those experimentally obtained is expected.

## 2. Materials

The studied materials are different NiCr alloys. With the purpose of better understanding the stress distribution in the substrate, several samples were designed. First, there are two shapes: a rectangle with a geometry of 6x6x0.4 mm, and a cylinder with a geometry of Ø6x0.9 mm. In order to name the samples more easily, code names are given in Table 1 for the samples with different shapes and oxidation conditions.

Table 1. Code names for the samples

| Code name | Shape | Size | Oxidation temperature | Oxidation time |
|---|---|---|---|---|
| Cyl_T1000_1h | cylinder | Ø6x0.9 mm | 1000 °C | 1 h |
| Cyl_T1000_5h | cylinder | Ø6x0.9 mm | 1000 °C | 5 h |
| Rec_T900_10h | rectangle | 6x6x0.4 mm | 900 °C | 10 h |
| Rec_T800_10h | rectangle | 6x6x0.4 mm | 800 °C | 10 h |

For cylinder samples, the chemical composition is a Ni-based alloy with a weight percentage of 28.28% Cr marked as Ni28Cr. For rectangular samples, whose chemical composition has a weight percentage of 34.5% Cr marked as Ni35Cr. These two materials are alloys that are resistant to oxidation and their behaviors after different oxidation conditions have extensively been studied [4-6]. Their chemical composition (percentage by weight) is shown in Table 2.

Table 2. Chemical composition (weight percentages)

| Ni28Cr alloy | Ni | Cr | Si | Mn |
|---|---|---|---|---|
| | 71.2 | 28.28 | < 0.01 | < 0.01 |
| Ni35Cr | Ni | Cr | C | Al |

| | | | | |
|---|---|---|---|---|
| alloy | 63.5 | 34.5 | 1.025 | 0.95 |

The average grain size of samples is 24.9 μm +/- 14μm obtained by EBSD measurements.

In order to choose the appropriate oxidation conditions, the following criteria have been considered: the prevention of crack and insurance of adhesion between the oxide layer and the substrate, a sufficient thickness of oxide layer to generate significant residual stresses for measurement. During the preparation of the experimental phase, several preliminary tests have been done. The surface quality has been analyzed after oxidation at 1000 °C for 1 h, 5 h and 10 h. Some cracks can clearly be seen in the sample oxidized at 1000 °C for 10 h. By analyzing the oxide thickness, it has been decided to work with samples conditions leading to a thickness value of the oxide layer less than 2.16 μm (Table 3).

It has been previously evidenced, for the present materials, with experimental characterizations by Thermal Gravimetric Analysis [5, 10], that the oxide thickness $\boldsymbol{h_{ox}}$ follows a parabolic evolution with the oxidation time t:

$$h_{ox} = A_p\sqrt{t} \quad (1)$$

where $A_p$ is the parabolic kinetics parameter that varies with temperature T. Both materials have very similar kinetics. Using the given parabolic kinetics parameter $A_p$ from [11], Table 3 is obtained, which shows the predicted thickness of oxide layer for different temperatures and different oxidation times.

Table 3. Thickness of the oxide layer

| 1000 °C | | | | | | |
|---|---|---|---|---|---|---|
| Time (h) | 1 | 2 | 3 | 4 | 5 | 10 |
| Thickness (μm) | 0.97 | 1.37 | 1.67 | 1.93 | 2.16 | 3.05 |
| 900°C | | | | | | |
| Thickness (μm) | 0.32 | 0.45 | 0.55 | 0.64 | 0.71 | 1.01 |
| 800°C | | | | | | |
| Thickness (μm) | 0.19 | 0.27 | 0.33 | 0.38 | 0.43 | 0.60 |

Considering the thickness of the oxide layer, in order to prevent relaxation phenomena such as cracking and maintain adhesion between the oxide layer and the substrate, it is not advisable to have long time oxidation, and thus to have a too thick layer. It should also not be too thin, at very short oxidation time, so that it does not generate significant residual stress in the system. Previous works [6,12] show that 1h oxidation under 1000 °C is sufficient for generating residual stress of about -400 MPa in oxide layer, which means that the thickness around 1 μm is well adapted. For 1000 °C the oxide layer grows faster than at 900 °C and 800 °C, so that 1 h and 5 h for oxidation time has been chosen. For 900 °C and 800 °C, the oxidation time 10 h is chosen in order to have roughly the same thickness.

## 3. High-energy synchrotron X-rays in transmission mode

### 3.1. Experimental setup

Basically, X-ray in transmission mode and X-ray in reflection mode share the same principles and are used to obtain information from materials. For example, XRD is widely applied to determine the elastic deformation of crystalline materials [13-15]. X-rays in transmission mode can be used to determine the residual stress distribution in substrate as a function of depth. The X-rays in transmission mode was used to determine the lattice parameters as a function of depth for Thermal Barrier Coatings, which is related to the depth-dependence of strain [9]. Transmission XRD and

reflection XRD also share the same principles to calculate stress [16, 17]. A comparison between the conventional Bragg-Brentano diffractometer and the two-dimensional XRD showed that the high-energy two-dimensional diffraction provides more information than conventional diffractometer and can be used to determine stress [18]. This setup has less limitation compared to reflection mode: no material removal, so no strain/stress relaxation and no depth limitation in the direction perpendicular to the gradient.

Experiments have been presently conducted at PETRA P07-EH2 beamline (DESY-Petra III, Hamburg, Germany). A high-energy beam (E=103.4 keV) with a rectangular shape and a small dimension along the vertical axis obtained using lenses (300x2 $\mu m^2$) has been used, coupled with a continuous vertical translation at 10 microns/s and a fast 2D Perkin-Elemer detector (pixels : 150x150 $\mu m^2$) with a frame rate of 10 Hz. It allows to obtain 2D images (2048x2048 pixels) containing full Debye-Scherer rings, every micron step corresponding to a diffraction volume of 300x(sample size)x3 $\mu m^3$. Detector has been placed at 1.5 m from the sample. Sample top surface has been aligned with the beam using rocking curves and absorption scans for different orientations around the vertical axis.

In the present experiments, the sample size and the beam size allows defining the grain number. By taking into account the pixel resolution, the multiplicity, the rocking curve width and assuming uniform orientation distribution of grains, it would be possible to give an estimation of this grain number. However, we have a beam that moves continuously ant that has its own horizontal and vertical divergence, which should increase the number of diffracting grains. We only see the grains, which are in the diffraction position (therefore not all the possible grains) and we do not see all the possible visible peaks if the grains are well oriented (because of the multiplicity). Consequently, it is difficult to give an accurate value for the real number of grains contributing to the diffracted intensity and only a range is possible to give between 100 and 5000 grains.

Absorption has been recorded using a photo-diode placed in the direct beam. Setup was calibrated using a $CeO_2$ powder (NIST standard). Sample to detector distance and detector misalignment have been determined using pyFAI software [19]. Calibrating powder and sample has been placed at the same position using a camera looking on sample top surface and performing absorption scans along x and y directions. Motor resolution for rocking curves was set to 0.005°, meaning that the final alignment is better, due to the high number of points in the scan (30 above Full Width at Half Maximum typically); so the required resolution can be easily reached with the setup for 1 μm resolution along z direction. As mentioned, all sources of misalignment will cause a change in strain/stress gradient determination, but the resolution of the setup is largely sufficient for our experiments. Samples was glued on an aluminum holder. The top sample surface was aligned using the direct beam and a photo-diode placed behind the sample. Several absorption and rocking curve scans have been performed to place the surface as flat as possible with respect to the beam.

Stress can be determined using the $\sin^2\psi$ method, knowing the radiocrystallographic elastic coefficients, provided in Table 5. As the materials consist of randomly oriented crystallites, Bragg's law is applied to evaluate the changes in lattice spacing between crystallographic planes, taking into account the diffraction geometry (Fig. 1). The aspect ratio does not influence significantly the method.

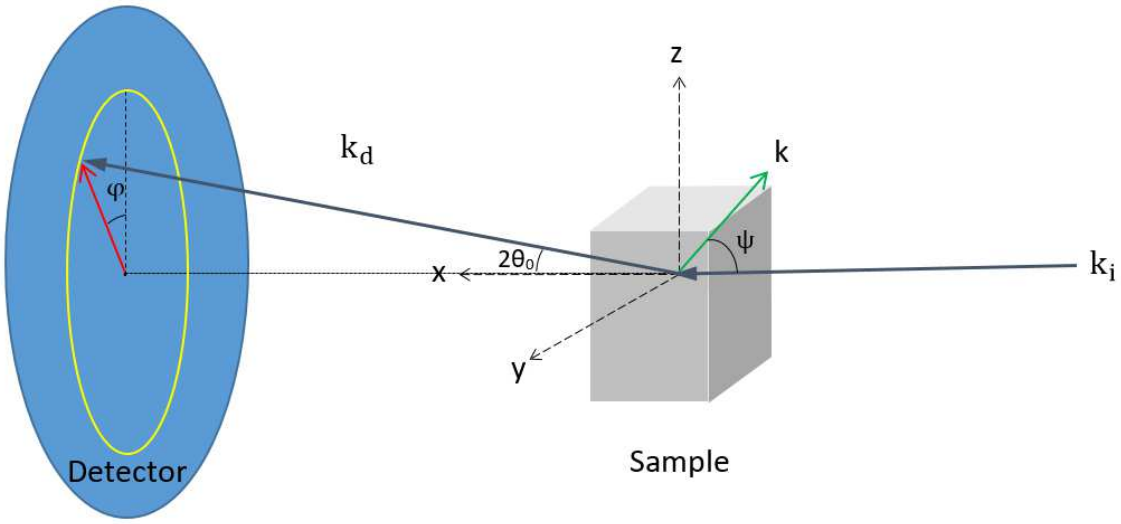


Figure 1. Geometrical configuration of the experiments ($k_i$ is the incident wave vector, $k_d$ is the diffracted wave vector)

The direction $\vec{e}_{\varphi\psi}$ is the normal to the diffracting planes, where ψ is the angle between the normal to the surface and the normal to the diffracting planes, and $\varphi$ is the angle between the vertical passing through the position of the direct beam and a given position on the diffraction ring. $2\theta_0$ is the angle between the incident beam and the diffracted beam, theoretically obtained for stress-free samples and provided in Table 5.

The raw data (see an example in Fig. 2) is an image of the diffraction ring. Picture is shown for a certain intensity scale. This choice influences the contrast of the picture. Consequently, the rings seem discontinuous whereas for a lower scale maximum value, the rings are indeed continuous with superposition of spots. Further data processing are required to obtain the corresponding stress.

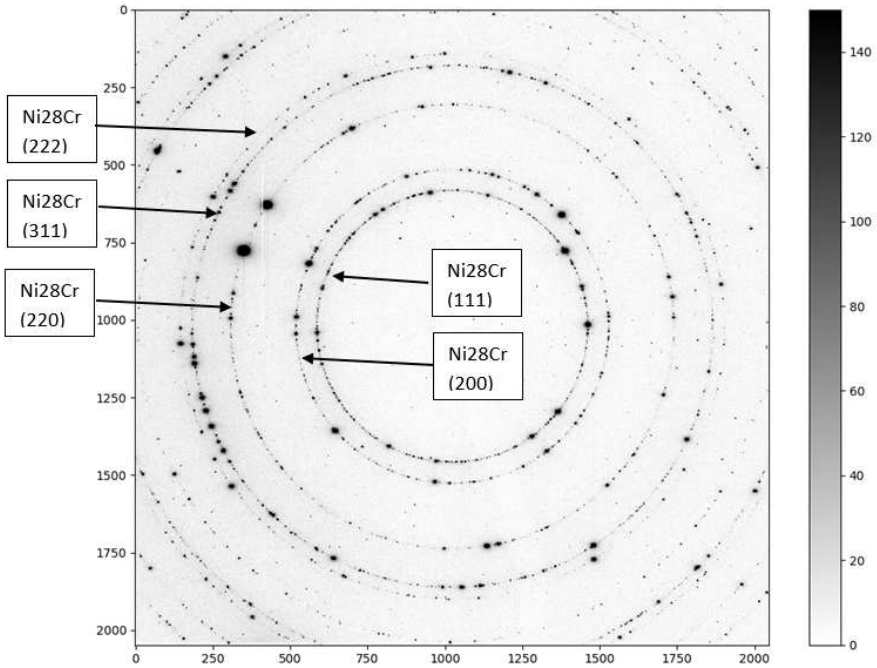

Figure 2. Diffracted rings for Ni28Cr substrate

Pixels size of the Perkin-Elmer detector is 150 μm. With a 6 mm sample, there exist a smear of the diffracting peaks over several pixels (around 4 in our case); the Full Width at Half Maximum is affected by the size of the sample, but not the position, which is used for present the analysis. The shape of the peaks used in the analysis remains symmetric and consistent with the function used to adjust them. The 2D pattern show several spots due the grain size of the NiCr alloy compared to the beam size. In the procedure to extract peak information (position, intensity, shape), selection steps are present to only select data from good adjustment of function to the experimental data. According to the intensities change, some parts of the data add distortion on the results. Caking steps as well as checking for adjustment process enable then to obtain a minimum statistics. Previous works have already highlighted these effects [6, 12].

In order to analyze the untreated data, the rings were subdivided into 90 sectors $\gamma$ whose values are between -180° and +180° with a step of 4°. From these data, it is possible to plot the intensities of each sector $\gamma$ as a function of $2\theta$, giving a 1D diffraction diagram. For metal layer, the peaks (111), (200), (220), (311) and (222) were tested. The peaks that have a better behavior are (311) and (222), which have the less punctuated distribution and a signal, for each gamma, which is more homogeneous.

After the subdivision of the rings, the choice of the best fitting method is the same as with the classical $\sin^2\psi$ method, including testing different distribution functions, fitting with or without background etc.

In that case, the simulation results are quite similar for the parameters obtained such as the intensity, the position, and the width of the peak. In order to choose the best function, we need to test systematically this procedure by considering a big number of experimental data. All this procedure has been automatized in a Matlab handmade software with the implementation of validity criteria on the fitting quality.

To simulate the background noise, a polynomial function is chosen whose order need to be tested. In the test, the peak and the background noise can be simulated together or separately. Several quality indicators are considered, such as:

- Mean value indicator: it is an indicator on the average stress value, which is calculated from the stresses obtained from the different methods. The mean value indicator represents a comparison of the mean stresses of the different methods.

- Variance indicator: it represents the difference between the results and average stress value. It is the most important parameter for smoothing the curve. When the variance indicator value is smaller, the curve is more convergent and smoother, which is exactly what we expect.

- Difference between maximum and minimum indicator: it is an indicator of the difference between the maximum and minimum values. The difference between maximum and minimum indicator is also an important parameter for smoothing the curve and for controlling the stress interval. However, it is less important than the variance indicator.

By applying this procedure for at least 100 pictures and after comparing these quality indicators, we consider that a Pearson 7 distribution function simultaneously with a background simulated by an order 3 polynomial leads to a correct minimization satisfying all the quality indicators. Therefore, this distribution has been considered for the simulation of all the data.

During the fitting of peaks, additional criterions were applied for limiting the abnormal points. First, for each peak, the theoretical values are set before the fitting, such as theoretical peak position,

expected peak width and expected peak intensity. In order to evaluate the quality of the fitting, the criterions are considered such as position criterion, width criterion and intensity criterion to limit abnormal point that would exceeds an absolute difference between theoretical values and experimental ones defined through thresholds. By optimizing these criterions, the most confident data is obtained. After limiting the abnormal points, the $\sin^2\psi$ curves are plotted and contain as a result between 20 and 45 points. Because of the data processing that degrades the grain statistics, some points may present a scattering effect even if the average representativeness is preserved.

The cleaning of the results eliminates automatically the most extreme peaks, with too high discrepancies in terms of intensity, position or FWHM of the peaks; and therefore it remains only the caking sectors where the applied method gives the best results, therefore where the number of grains is a priori sufficient. Details on the data processing, especially to select correct peaks as well as removing aberrant points in the $\sin^2\psi$ curves, can be found in [6,12].

Using synchrotron setup means that the method has to be adapted to the beamline, detection method, sample and purpose. The comparison between our setup and purpose with other methods using laboratory device or low energy synchrotron setup on dedicated beamline with material removal [20], or technique to detect gradient over a depth of 100µm [21, 22, 23] can be done.

The data processing is similar to the one performed in reflection mode, which has been widely discussed in [6, 12]. As it can be seen in Fig.1, the quality of different rings varies considerably. The diffraction rings have been divided into several sectors of 4°. For each sector, the integration of intensity as a function of $\boldsymbol{2\theta}$ was calculated. By choosing the best method to fit the peaks and reject abnormal values, the values $\boldsymbol{2\theta}$ can be obtained, which have a shift from the values $\boldsymbol{2\theta_0}$, due to mechanical stress in the sample. A small positive stress is expected in metal layer. By analyzing all the peaks from the rings caking, only the most interesting peaks are presented. Because the material is not perfectly isotropic and homogeneous, the signals from different peaks are not exactly the same, such as Full Width at Half Maximum, intensity of peak etc. Moreover, the signal quality of different peaks is different. For a better signal quality and smaller errors, only the results from the ring (311) are presented. This aspect was investigated in previous publications, such as [4].

3.2. Data processing for stress determination

When a material is deformed, the lattice spacing between the crystallographic planes $\boldsymbol{d_{hkl}}$ expands or contracts, causing a shift in the position of the rings in the diffraction pattern. Changes in the lattice spacing between the crystallographic planes can be evaluated as a result by measuring this angular shift, which can then determine the elastic deformation.
The strain on the direction $\vec{\boldsymbol{e}}_{\varphi\psi}$ is:

$$\varepsilon_{\psi\varphi} = \vec{\boldsymbol{e}}_{\varphi\psi}.\acute{\varepsilon}.\vec{\boldsymbol{e}}_{\varphi\psi} \quad (2)$$

with

$$\vec{\boldsymbol{e}}_{\boldsymbol{\varphi\psi}} = -\boldsymbol{cos\psi}\vec{\boldsymbol{e}}_{\boldsymbol{x}} + \boldsymbol{sin\psi sin\varphi}\vec{\boldsymbol{e}}_{\boldsymbol{y}} + \boldsymbol{sin\psi cos\varphi}\vec{\boldsymbol{e}}_{\boldsymbol{z}} \quad (\mathbf{3})$$

and $\acute{\varepsilon}$ is the elastic strain tensor, with the assumption that there is no shear strain (this assumption has been verified for the current experiments and has already been notified on similar previous experiments [4,12]):

$$\acute{\varepsilon} = \begin{pmatrix} \varepsilon_{xx} & 0 & 0 \\ 0 & \varepsilon_{yy} & 0 \\ 0 & 0 & \varepsilon_{zz} \end{pmatrix} \quad (4)$$

The strain along the direction $\vec{e}_{\varphi\psi}$ can be developed as:

$$\varepsilon_{\psi\varphi} = cos^2\psi\varepsilon_{xx} + sin^2\psi sin^2\varphi\varepsilon_{yy} + sin^2\psi cos^2\varphi\varepsilon_{zz} \quad (5)$$

The actual true/rational strain along the direction $\vec{e}_{\varphi\psi}$ can also be calculated by comparing the undeformed lattice spacing $d_0$ between the crystallographic planes with the deformed lattice spacing d.

$$\varepsilon_{\psi\varphi} = ln\left(\frac{d}{d_0}\right) = ln\left(\frac{sin\theta_0}{sin\theta}\right) \quad (6)$$

Bragg's law provides the last equality. It provides, through the combination of Eq.5 and Eq.6, a linear relationship between $ln(1/sin\theta)$, calculated with the angular shift (from $\theta_0$ to $\theta$), and the elastic strain.

$$ln\left(\frac{sin\theta_0}{sin\theta}\right) = cos^2\psi\varepsilon_{xx} + sin^2\psi sin^2\varphi\varepsilon_{yy} + sin^2\psi cos^2\varphi\varepsilon_{zz} \quad (7)$$

Because of the geometry configuration, the direction of measurement is the bisector between the incident beam and the diffracted beam. However, the undeformed geometric configuration is considered:

$$\psi \approx \frac{\pi}{2} - \theta_0 \quad (8)$$

This approximation holds if the strain does not shift significantly the ring. The usual $sin^2\psi$ strain relationship is now considered as a $sin^2\varphi$ strain relationship.

$$ln\left(\frac{1}{sin\theta}\right) = sin^2\theta_0\varepsilon_{xx} + cos^2\theta_0 sin^2\varphi\varepsilon_{yy} + cos^2\theta_0 cos^2\varphi\varepsilon_{zz} - ln(sin\theta_0) \quad (9)$$

Under the assumption that the elasticity of the material is linear, homogeneous and isotropic, the conversion of elastic strain to stress can be performed using Hooke's model according to:

$$\acute{\varepsilon} = \frac{1+\nu}{E}\acute{\sigma} - \frac{\nu}{E}trace(\acute{\sigma})\acute{I} \quad (10)$$

where trace($\acute{\sigma}$) is the first invariant of the stress tensor and $\acute{I}$ is the three-dimensional (3D) identity tensor.

The shear stress is not considered according to previous works [6, 12]. From those previous studies, with such a material NiCr under the thermochemical loading, we experimentally know that the shear is negligible compared to the other stress components. In other words, the coordinate system along the geometry is proper and leads directly to eigenstresses. In addition, a stress gradient along axis z is considered through the presence of a normal stress $\sigma_N$. Leading to an isotropic in-plane stress state, the tensor $\acute{\sigma}$ should be:

$$\acute{\sigma} = \begin{pmatrix} \sigma & 0 & 0 \\ 0 & \sigma & 0 \\ 0 & 0 & \sigma_N \end{pmatrix} \quad (11)$$

By applying the radiocrystallographic elastic coefficients $S_{ij}$, the $\sin^2\boldsymbol{\varphi}$ relation becomes:

$$\boldsymbol{ln\left(\frac{1}{sin\theta}\right) = \frac{1}{2}S_{2(hkl)}(\sigma - \sigma_N)cos^2\theta_0 sin^2\varphi + \frac{1}{2}S_{2(hkl)}\sigma + S_{1(hkl)}(2\sigma + \sigma_N) + \frac{1}{2}S_{2(hkl)}(\sigma_N - \sigma)cos^2\theta_0 - ln(sin\theta_0)} \quad (12)$$

Plotting the curve $\boldsymbol{ln\left(\frac{1}{sin\theta}\right)}$ as a function of $\boldsymbol{sin^2\varphi}$ gives us:

$$\begin{cases} \boldsymbol{Slope: A = \frac{1}{2}S_{2(hkl)}(\sigma - \sigma_N)cos^2\theta_0} \\ \boldsymbol{Intercept: B = \frac{1}{2}S_{2(hkl)}\sigma + S_{1(hkl)}(2\sigma + \sigma_N) + \frac{1}{2}S_{2(hkl)}(\sigma_N - \sigma)cos^2\theta_0 - ln(sin\theta_0)} \end{cases} \quad (13)$$

By solving this two variables linear equations, the stresses $\boldsymbol{\sigma}$ and $\boldsymbol{\sigma_N}$ can be obtained:

$$\begin{cases} \boldsymbol{\sigma_N = \frac{B + ln(sin\theta_0) - \frac{\beta_2 A}{\beta_1}}{\beta_2 + \beta_3}} \\ \boldsymbol{\sigma = \sigma_N + \frac{A}{\beta_1}} \\ \boldsymbol{with} \\ \boldsymbol{\beta_1 = \frac{1}{2}S_{2(hkl)}cos^2\theta_0} \\ \boldsymbol{\beta_2 = 2S_{1(hkl)} + \frac{1}{2}S_{2(hkl)}(1 - cos^2\theta_0)} \\ \boldsymbol{\beta_3 = S_{1(hkl)} + \frac{1}{2}S_{2(hkl)}cos^2\theta_0} \end{cases} \quad (14)$$

The radiocrystallographic elastic coefficients (Table 5) for the different families of planes (hkl) has been considered and the initial position of $\boldsymbol{2\theta_0}$ (Table 5) can be calculated from the values given in [29, 30].

Table 5. Radiocrystallographic elastic coefficients and initial position $\boldsymbol{2\theta_0}$ for different families of planes (hkl)

| Plane (hkl) NiCr | $S_1$ (hkl) ($TPa^{-1}$) | $0.5S_2$ (hkl) ($TPa^{-1}$) | $\boldsymbol{2\theta_0}$(°) at E=103.4 keV |
|---|---|---|---|
| (311) | -17.693 | 54.472 | 6.496 |
| (222) | -1.122 | 4.760 | 6.785 |

It has been shown that there is a relationship between the observed diffraction pattern ($\boldsymbol{2\theta}$) when X-rays are diffracted through the crystal lattices and the lattice spacing between the crystallographic planes *d* within the material. The interplanar spacing $\boldsymbol{d_0}$ of a stress-free material produces a characteristic diffraction pattern ($\boldsymbol{2\theta_0}$) for this material. By changing the interplanar spacing, different diffraction patterns can be obtained. This induced change in crystallographic planes causes a shift in the diffraction pattern. Precise measurements of this angular shift allow to evaluate the changes in interplanar spacing and thus to deduce the stress in the material by use of Eq. 14. The translation of the strain resolution (around 1E-4 corresponding to camera resolution) to stress resolution can be roughly obtained by inverting Eq. 10 and using radiocrystallographic elastic coefficients from Table 5. It leads to 72 MPa that is smaller than the given error range.

We can wonder about the origin of the stress distribution. It is hard to distinguish if the stress distribution is caused by chemical/diffusion strain or different stress-free lattice parameter that would be essentially caused by chromium depletion. However, the $\boldsymbol{2\theta_0}$ values have been carefully checked following previous works. Indeed, the effect of the chromium concentration on $\boldsymbol{2\theta_0}$ has been investigated in [12]. We had shown that the (stress free) interreticular spacing does not seem to significantly depend on chromium content. In the present work, the oxidation time and temperature (see in Table 3) lead to the same chromium depletion content. Moreover, our present proposition of influence of chromium diffusion on residual stress further show that the length of diffusion is eventually smaller than the gradient of residual stresses that also proves that the effect of chromium on undeformed lattice spacing would not explain all the observations along all the depth.

## 4. Modelling for {metal+oxide} system

In previous works [12, 25], the thermomechanical modelling for {metal+oxide} system has been established. The modelling is proposed under the following hypotheses:

- The mechanical state of the system is in-plane isotropic according to the Eqs. 4 and 11. In the metal, further results are confirming this assumption (see in section 5.2). Instead of previous works, we have presently considered the stress for normal direction. In general, not only around the interface, it is reasonable to assume a general non-isotropic stress and strain tensors;
- The oxide has homogeneous mechanical state. In the present case, 1 μm of oxide layer is obtained under the time and temperature of oxidation. Because a 2 μm of beam size is considered in the vertical direction (perpendicular to the top sample surface), the experimental measurements were necessarily averaging the information from the oxide layer. This assumption is presently tested in the metal through the considered experiments;
- For all the materials, the behavior is isotropic and homogeneous. The behavior of materials is at least thermo-elasto-viscoplastic with additional specific behavior in oxide due to growth.

The strain in this modelling contains four parts, which are: elastic part, viscoplastic part, thermomechanical part and growth strain part only for the oxide layer. Because of the adherence between oxide layer and metallic substrate, the continuity equation can be expressed as, for all oxidation time:

$$\varepsilon_m = \varepsilon_{ox} \tag{15}$$

where $\varepsilon_m$ is strain in the metal layer and $\varepsilon_{ox}$ is strain in the oxide layer.
Eq.15 can also be presented with the following decomposition:

$$(\varepsilon^{elastic} + \varepsilon^{viscoplastic} + \varepsilon^{thermal})_m = (\varepsilon^{elastic} + \varepsilon^{viscoplastic} + \varepsilon^{thermal} + \varepsilon^{growth})_{ox} \tag{16}$$

The expression of each component can be found in [12, 25]. Even though, in this article, the samples are oxidized under isothermal condition, the component $\varepsilon^{thermal}$ is not equal to 0 leading to residual stresses developed during cooling, which are then measured at room temperature. In other words, the thermal loading of the system is not fully isothermal and may also play a role in the mechanical balance.

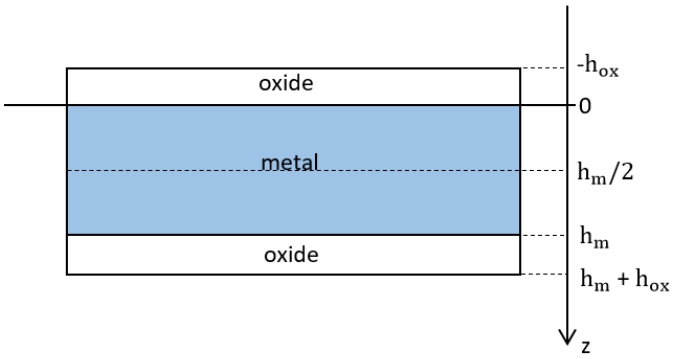


Figure 3. Geometry for the oxide growing on a metal

Fig. 3 shows the geometry for the oxide growth on a metal, which gives us the equation of mechanical balance:

$$\int_0^{h_m} \sigma_m(z)dz + \int_{-h_{ox}}^{0} \sigma_{ox}\, dz + \int_{h_m}^{h_m+h_{ox}} \sigma_{ox}\, dz = 0 \quad (17)$$

where $\sigma_{ox}$ is the stress in the oxide, $h_{ox}$ is the oxide thickness that depends on time t, $\sigma_m(z)$ is the stress in the substrate that depends on z, and $h_m$ is the thickness of the substrate. The stress in metal $\sigma_m(z)$ is considered as a function of depth z. The stress in oxide is considered as a constant according to the assumption. The geometry is a three layers system, which is {Oxide + Metal + Oxide}. Moreover, the system is symmetrical with respect to the median plane. Therefore, Eq.17 will be further simplified into Eq.19.

## 5. Results and analyses

### 5.1 Comparison between stress $\boldsymbol{\sigma}$ and $\boldsymbol{\sigma_N}$

First, by using the method described above (Eq. 14 in section 3.2), the stress-depth curves in metal are obtained. The in-plane stress $\boldsymbol{\sigma}$ and normal stress $\boldsymbol{\sigma_N}$ can be clearly presented by overlapping them in the same figure (Fig.4).

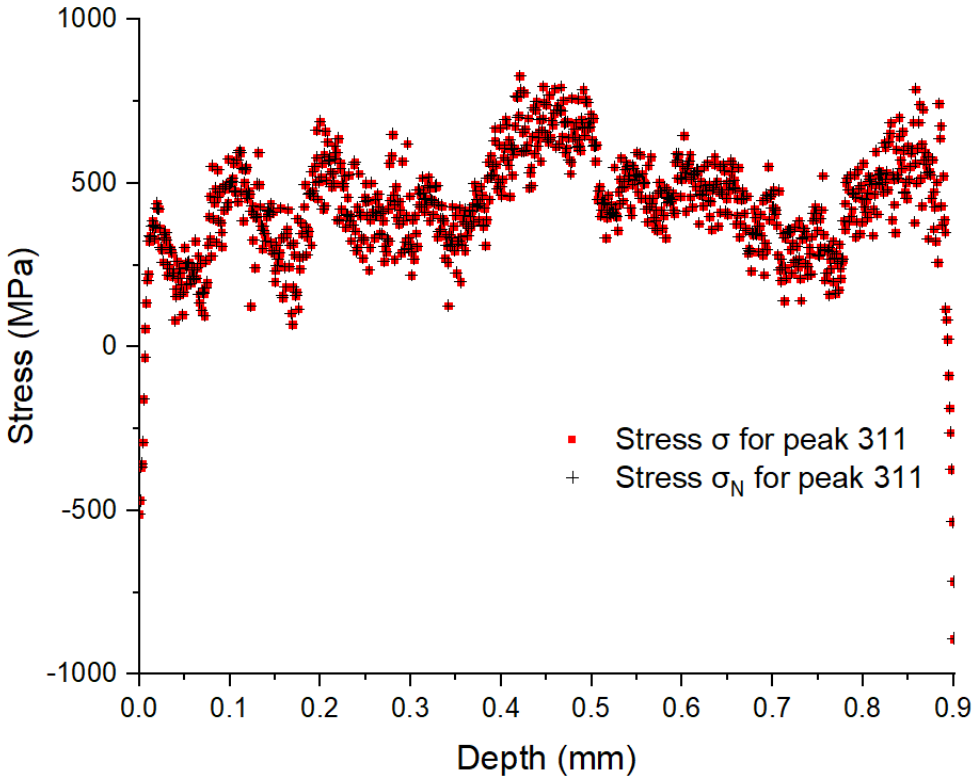


Figure 4. Stress $\boldsymbol{\sigma}$ and $\boldsymbol{\sigma_N}$ for peak (311) of sample Cyl_T1000_1h

Fig.4 compares stress $\boldsymbol{\sigma}$ and $\boldsymbol{\sigma_N}$ for peak (311) of sample Cyl_T1000_1h at rotation direction 0°. The overlap clearly indicates that the stress $\boldsymbol{\sigma}$ and $\boldsymbol{\sigma_N}$ are identical in the metal. From the data processing point of view, the term $\frac{\boldsymbol{A}}{\boldsymbol{\beta_1}}$ in Eq. 14 is very small, which leads to the stress $\boldsymbol{\sigma}$ and $\boldsymbol{\sigma_N}$ to be similar in the metal. It does not contribute significantly to the value of the out-plane stress. It is worth noting that this distribution of stresses are proposed/measured only in the metal (under the measurement uncertainties). However, for the metal layer, the normal stress usually appears with the planar stress evolution. Similar results have been obtained for all the samples. According to these obtained results, a relation between in-plane stress $\boldsymbol{\sigma}$ and normal stress $\boldsymbol{\sigma_N}$ in the metal is proposed for the investigated materials:

$$\boldsymbol{\sigma_{xx} = \sigma_{yy} \approx \sigma_{zz}} \quad (\mathbf{18})$$

where $\boldsymbol{\sigma_{xx}, \sigma_{yy}}$ equals to in-plane stress $\boldsymbol{\sigma}$, and $\boldsymbol{\sigma_{zz}}$ equals to normal stress $\boldsymbol{\sigma_N}$.

Because the system is not in general a priori isotropic, there is not only hydrostatic stress in such a system. There are in-plane and out-plane stresses, both in the metal and in the oxide, that a priori can depend on the z position especially for the metal, whereas for the oxide it can be considered as constant at first-order approximation. Indeed, from an experimental point of view, the oxide layer is too thin to consider a stress distribution along axis z and is thus considered as homogeneous. Mechanical balance is thus considered in such a system.

Previous modelling takes into account only in-plane stress (i.e. out-plane stress = 0), whereas in the present study we also consider the out-plane stress). An in-plane stress is assumed for the oxide layer because the thickness is too thin of the order of 1 μm, as performed in previous works [12, 25]. Such a hypothesis of in-plane stress for the oxide layer is not fully satisfying, which may bring a lack of

continuity of the normal stress at the oxide/metal interface. Another consequence is that the thickness of oxide layer is so thin that the stress gradient in the oxide is generally ignored. On the contrary, the substrate has a larger thickness. For sample Cyl_T1000_1h, the thickness is 0.9 mm, which is around 900 times thicker than the thickness of oxide layer. The equation of mechanical balance and recent work [12] confirm that the stress in oxide layer is compression and the stress in metal layer is tension, which are opposites ones, for the considered systems. Thus, the existence of stress gradient as a function of depth is possible, especially in the near interface zone. This is confirmed in Fig. 4 and has been observed for all the samples.

Ideally, the stress-depth curve should be a curve symmetrical with respect to the middle plane, because of the symmetrical geometry, the identical oxidized conditions, the same measurement process etc. As shown in Fig.4, the stress distribution is observed roughly symmetric to the central plane, especially when focusing at the stress distribution near the top and bottom surfaces. However, due to the bonding between the sample and sample holder, we can observe signal differences at the bottom surface. In addition, at the bottom surface, the signal can be polluted by information providing from the sample holder. Therefore, only the top half part will be presented, including the top surface and the stress distribution down to the central plane. Assuming the symmetry of the system and considering only half of the information, the equation of mechanical balance should be now approximately considered as:

$$\int_{0}^{h_m/2} \boldsymbol{\sigma_m(z)dz} + \int_{-h_{ox}}^{0} \boldsymbol{\sigma_{ox}\, dz} = \mathbf{0} \quad (\mathbf{19})$$

5.2 Comparison between different rotation directions

For each sample, three directions of penetration have been applied: 0°, 90° and -90°, which are related to the sample position rotation around the z axis (Fig.1). Normally, -90° and 90° should be equivalent because of the same X-ray beam path.

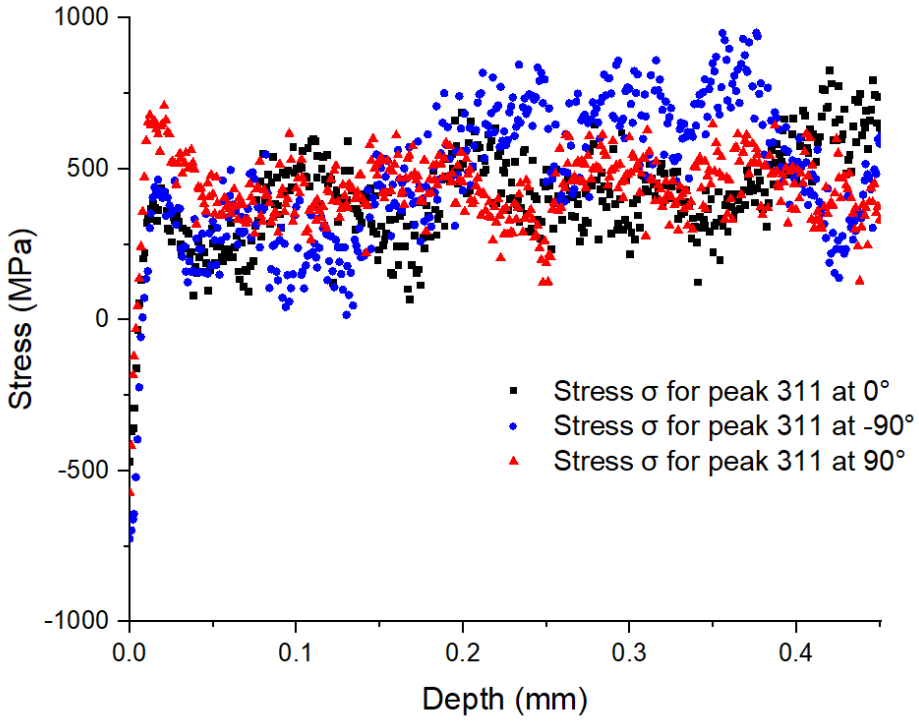

Figure 5. Stress $\boldsymbol{\sigma}$ for three rotation directions for peak (311) of sample Cyl_T1000_1h

As shown in Fig.5, the stresses between different rotation directions are quite similar. The response to a same X-ray path should be theoretically the same. However, there are differences between different rotation directions, even for -90° and 90°. This may be explained by instrumentation errors or beam variations when rotating the sample, as well as possible heterogeneities of the alloy depending on the X-ray path (between 0° and 90°). No significant difference in the trends of the stress distribution was found between these three directions of rotation, especially at the near surface part where a stress gradient is systematically observed. So that we can consider that the stress state is isotropic but heterogeneous in the metallic substrate.

In order to investigate the stress distribution as a function of depth, the mean stress of these three rotation directions has been calculated. In the meantime, the sample standard deviation is also obtained. Since there are only three directions of rotation, to investigate the mean stress of all directions, the sample standard deviation is used, which is presented as error bar in the further figures. The mean standard deviation of the sample in all the three directions is 153 MPa. This value can be considered as the maximum range of acceptable error.

5.3 Average stress as a function of depth

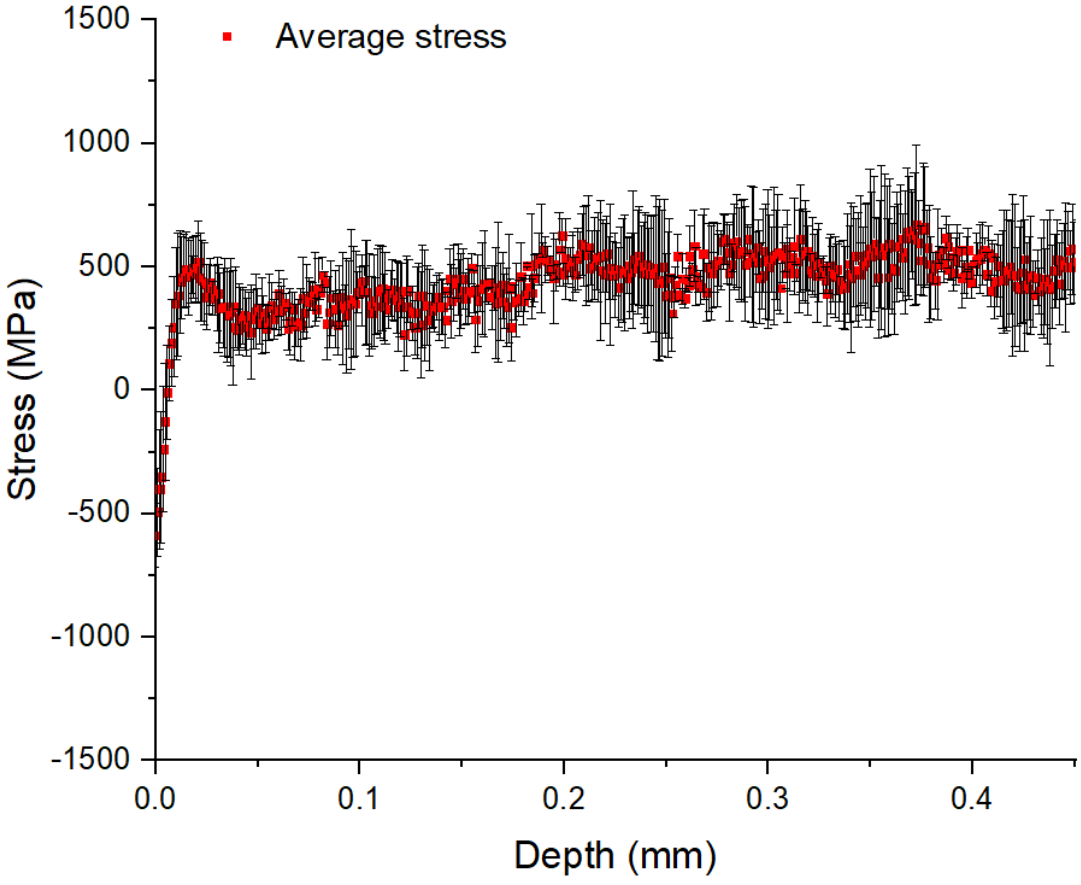


Figure 6. Average stress of three rotation directions for peak (311) as a function of depth of sample Cyl_T1000_1h.

Fig.6 presents the results for Cyl_T1000_1h. As shown in Fig.6, the distribution of stress $\boldsymbol{\sigma}$ as a function of depth is non-linear and roughly constant far from the interface. The sample standard deviation is calculated by three different rotation directions, which is shown as error bars in Fig.6. The minimum stress is at the top surface, which is -588 ± 128 MPa. Since the stress in the oxide layer is negative [12, 10] and expecting continuity of the normal stress (equal to the in-plane stress in the metal), it is reasonable that the stress in the substrate has a negative value near the interface. At depth 7 μm, the stress exceed 0 MPa. Because of the mechanical balance [12], the majority of stress in the metallic substrate should be positive. The stress indeed changes very fast from 0 to 10 μm, which changes from -588 ± 128 MPa to 384 ± 249 MPa. At this depth, the influence of the concentration of different elements is concerned, such as O, Cr and Ni [26-28]. For the system NiCr + $Cr_2O_3$, the cationic diffusion mechanism is considered, which means cationic $Cr^+$ transport outward the surface to form $Cr_2O_3$. Therefore, the depletion of Cr causes crystallographic defect such as vacancy defects, edge dislocation, etc. The crystallographic defect may produce strain and stress, which can be called diffusion stress.

After 10 μm, the majority stress distributes from 0 MPa to 500 MPa and the average stress of metal layer is 452.3 MPa. The average of sample standard deviation is 153 MPa.

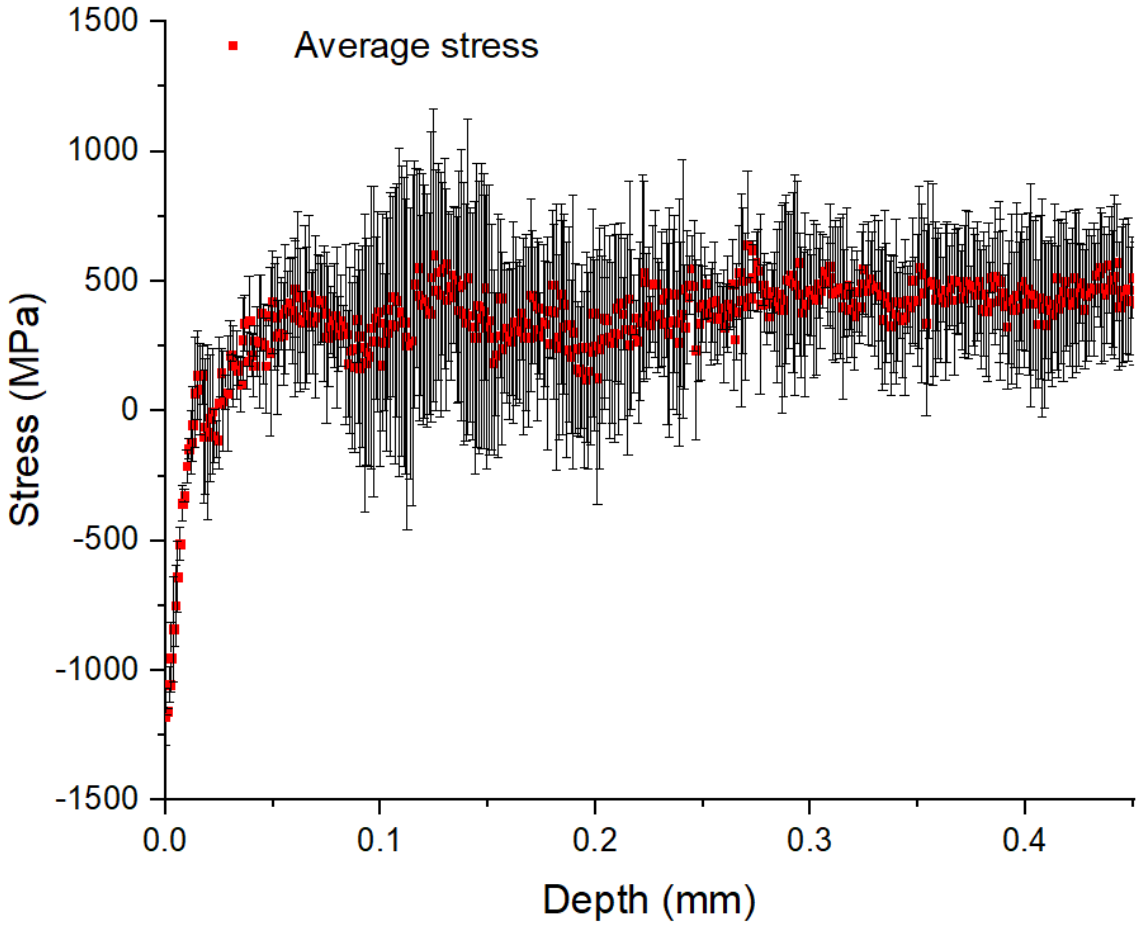


Figure 7. Average stress of three rotation directions for peak (311) as a function of depth of sample Cyl_T1000_5h.

Fig.7 presents the results for Cyl_T1000_5h. It shows that the minimum stress is -1179 ± 108 MPa at top surface, which is lower than the stress at the same depth of sample Cyl_T1000_1h. Because of longer oxidation time, the oxide thickness of sample Cyl_T1000_5h is thicker than sample Cyl_T1000_1h,

which causes a higher growth strain in oxide layer. The stress exceed 0 MPa at 14 µm, which is deeper than for sample Cyl_T1000_1h. After 14 µm, the majority stress then distribute from 0 MPa to 500 MPa and the average stress of metal layer is 388.8 MPa and the average of sample standard deviation is 274 MPa, which is higher than for sample Cyl_T1000_1h.

The values of the experimental stress may also present uncertainties, because of the measurements process, the dilatation correction and calibration procedure [12] that are not presently detailed. It also strongly depends on the numerical value of the stress-free Bragg's angle ($2\theta_0$). However, if the experimental results are considered in a relative way, for example by comparing ratio between different oxidation conditions, these results keeps a significant interpretation. The same tendency of stress distribution is repeatable for different oxidation times and for different oxidation temperatures, meaning that the spatial stress evolution with non-linear variation is a significant and important result of the present measurements.

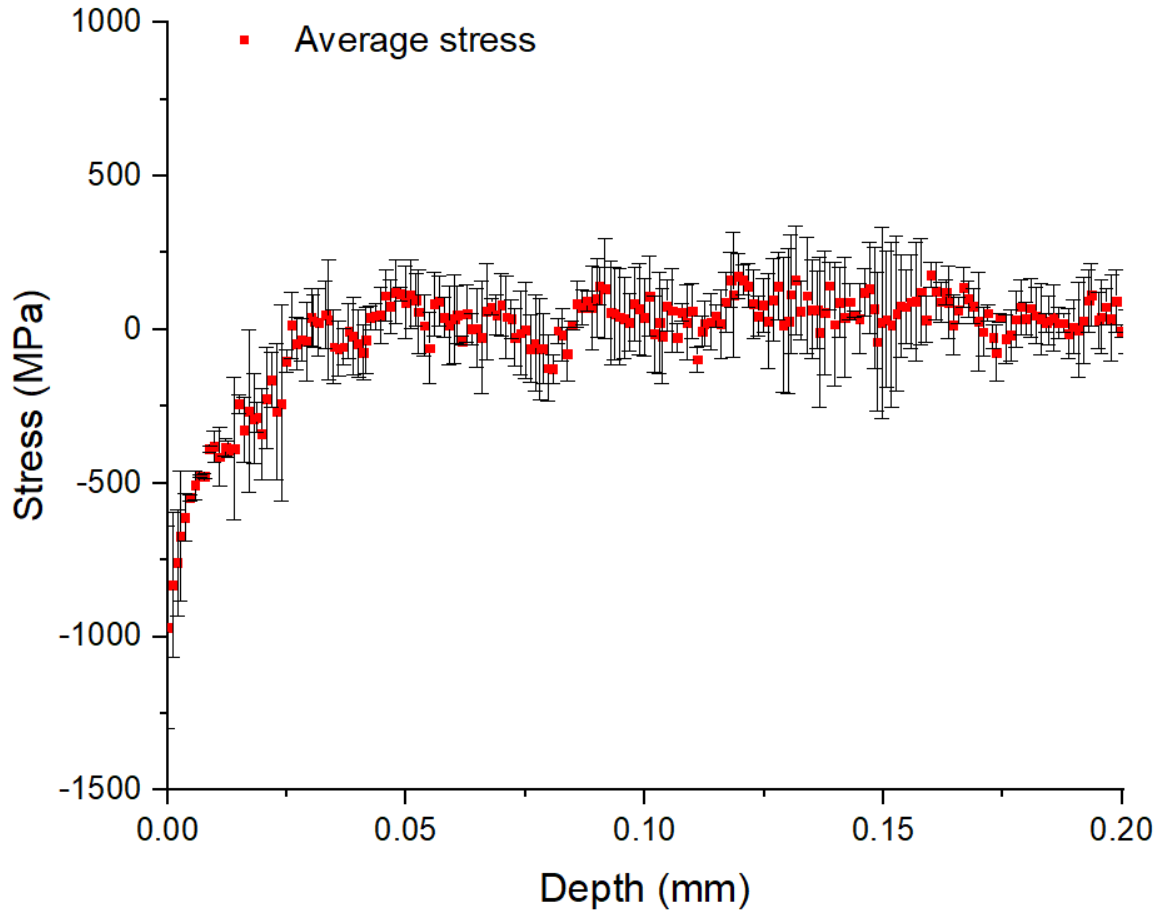


Figure 8. Average stress of three rotation directions for peak (222) as a function of depth of sample Rec_T900_10h.

Fig.8 shows that the stress distribution of sample Rec_T900_10h is quite similar to that of oxidized samples at 1000 °C. The minimum stress is -970 ± 329 MPa at top surface. It exceed 0 MPa at 26 µm. The majority stress is distributed from 0 MPa to 250 MPa with an average stress at 41.7 MPa, and the average of sample standard deviation is 120 MPa.

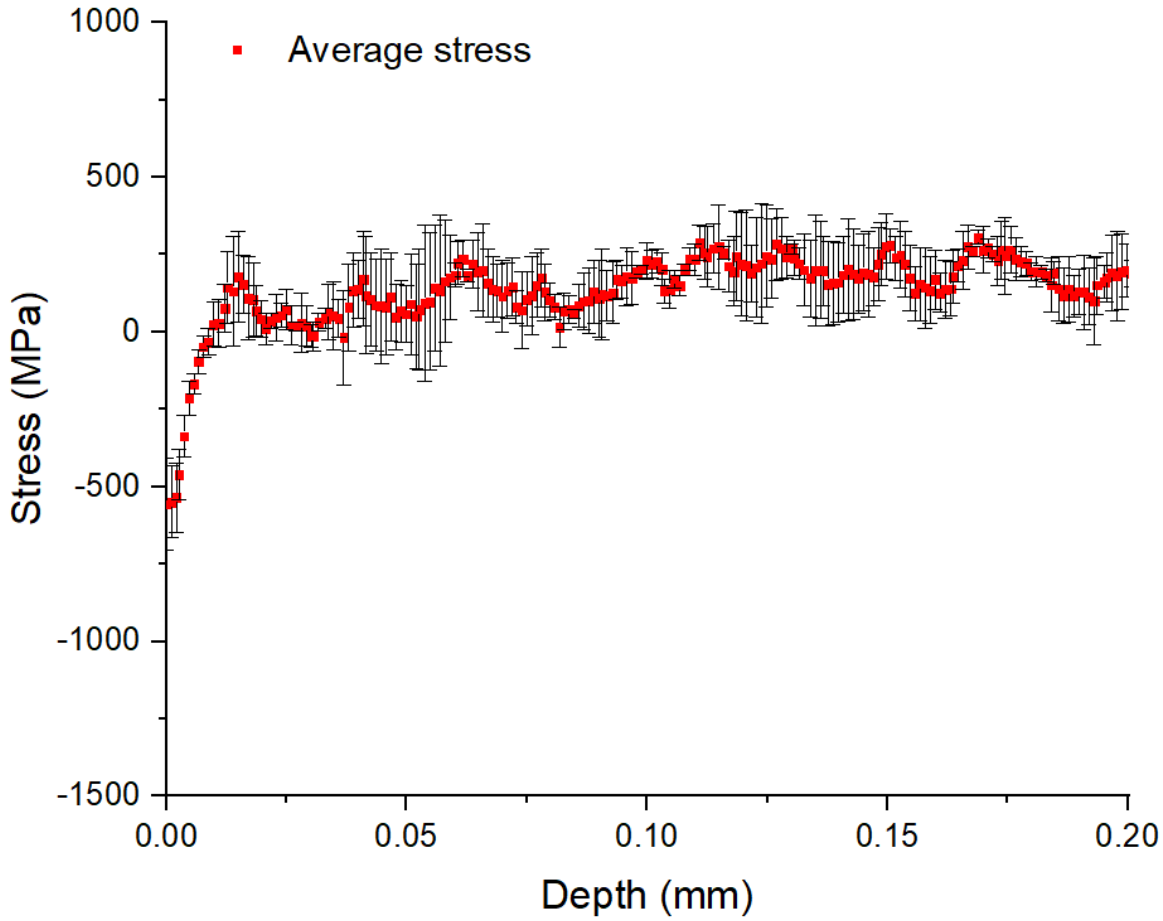


Figure 9. Average stress of three rotation directions for peak (222) as a function of depth of sample Rec_T800_10h.

As shown in Fig.9, for sample Rec_T800_10h, the minimum stress is -557 ± 148 MPa at top surface. It exceeds 0 MPa at 10 μm. After that, the stress mainly distributes from 0 MPa to 250 MPa with an average stress 151.5 MPa. The average of sample standard deviation is 97 MPa.

Table 6. Comparison of the four samples

| | Minimum stress at interface | Depth for 0 MPa | Average stress after depth for 0 MPa | Average of sample standard deviation |
|---|---|---|---|---|
| Cyl_T1000_1h | -588 ± 128 MPa | 7 μm | 452.3 MPa | 153 MPa |
| Cyl_T1000_5h | -1179 ± 108 MPa | 14 μm | 388.8 MPa | 274 MPa |
| Rec_T800_10h | -557 ± 148 MPa | 10 μm | 151.5 MPa | 97 MPa |
| Rec_T900_10h | -970 ± 329 MPa | 26 μm | 41.7 MPa | 120 MPa |

The resume of Fig.6 – Fig.9 (Table 6) indicates that the minimum stress appears at the oxide/metal interface. It shows with the same oxidation temperature, the longer oxide time, the lower minimum stress is reached; and with the same oxidation time, the higher oxidation temperature, the lower minimum stress is reached. For the depth of 0 MPa, the longer oxidation time or the higher oxidation

temperature, the depth is deeper. The depth of 0 MPa is related to the stress at interface, which is connected with the stress in oxide layer through the mechanical balance of the system, providing adhesion at the interface.

The average stress after depth of 0 MPa in metal part presents differences for cylinder samples and rectangle samples. However, comparing the samples of the same shape shows that the average stress after depth of 0 MPa is smaller for longer oxidation time and higher oxidation temperature, which means the relaxation of stress is more significant when the oxidation time is longer or the oxidation temperature is higher, at a given point in the metal.

## 6. Discussion on the stress distribution

### 6.1 Determination of diffusion coefficient

In order to analyze the stress distribution in the metallic substrate, a chemical/diffusion strain is introduced in the modelling, as the experience results shows that a stress gradient appears near the interface of metal and oxide layer. Indeed, in such materials, the concentration profile indicates that the concentration of chromium changes near the interface of metal and oxide layer in such a system [26-28], which has been proved to have an effect on the lattice spacing $d$ between the crystallographic planes within the material. This variation in Cr concentration is strongly related with local variations in diffraction pattern observed ($2\theta$), which will cause the stress gradient in metal layer. Thus, a chemical/diffusion strain is proposed.

To calculate the concentration profile of chromium, the 1D diffusion of Fick's law is used:

$$D\frac{\partial^2[Cr](z,t)}{\partial z^2}-\frac{\partial[Cr](z,t)}{\partial t}=0 \quad (20)$$

where $D$ is the chromium diffusion coefficient in the alloy; $[Cr]$ is the weight percentages concentration of element Cr, and z is the depth. The diffusion coefficient $D$ of element Cr in Nickel-Chromium alloys system has been studied in [27, 28]. In the work of Ruzickova, J et al.[27], the alloy used is Ni29.4Cr and the alloy is Ni30Cr in the work of Monma, K et al.[28], which are quite similar to the alloys studied in our present work. An Arrhenius law is proposed to describe the temperature dependence:

$$\boldsymbol{D=D_0 exp\left(\frac{-Q}{RT}\right)} \quad (\mathbf{21})$$

where $D$ is the diffusion coefficient, $\boldsymbol{D_0}$ is the pre-exponential factor, Q the activation energy, R the ideal gas constant and T the temperature. With the expression of $D$ (Eq.21), the figure of $ln(D)$ as function of 1/T has been plotted (Fig.10).

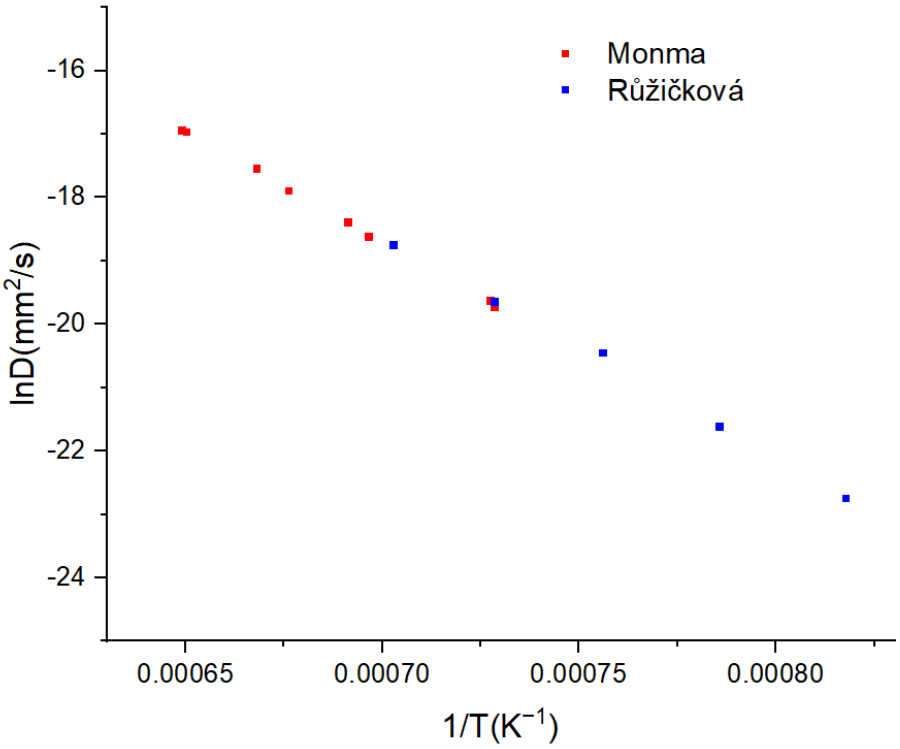


Figure 10. Diffusion data from the literature [27, 28]

Fig.10 provides an overview of linear relationship between ln(D) and 1/T. Therefore, the diffusion coefficient at 800°C, 900°C and 1000°C can be calculated (Table 7).

Table 7. Diffusion coefficient with $D_0$=297.5 mm2/s and Q=288.8kJ (calculated from Eq. 21 by using data from the literature [27, 28])

| T (K) | D (mm²/s) |
|---|---|
| 1073 | 2.59038E-12 |
| 1173 | 4.09273E-11 |
| 1273 | 4.19124E-10 |

6.2 Analyses of chromium concentration profiles

To analyze the concentration of chromium in our system, the initial condition (IC) and boundary conditions (BC) are considered as:

$$\begin{cases} \boldsymbol{IC}: \quad [\boldsymbol{Cr}]_{\boldsymbol{i}} = [\boldsymbol{Cr}](\boldsymbol{z},\boldsymbol{0}) = \boldsymbol{28.28\%} \vee \boldsymbol{34.5\%} \\ \boldsymbol{BC1}: \quad \dfrac{\boldsymbol{\partial}[\boldsymbol{Cr}](\boldsymbol{z},\boldsymbol{t})}{\boldsymbol{\partial z}} = \boldsymbol{0}, \boldsymbol{z} = \dfrac{\boldsymbol{h_m}}{\boldsymbol{2}}, \boldsymbol{0} < \boldsymbol{t} < \infty \\ \boldsymbol{BC2}: \quad [\boldsymbol{Cr}](\boldsymbol{0},\boldsymbol{t}) = \boldsymbol{\alpha}[\boldsymbol{Cr}]_{\boldsymbol{i}}, \boldsymbol{0} < \boldsymbol{t} < \infty \end{cases} \quad (\boldsymbol{22})$$

The initial condition indicates that at initial time, the weight concentration of chromium is 28.28% for all depth for cylinder samples and 34.5% for rectangle samples. The first boundary condition (BC1) indicates that at any time the rate of weight concentration for Cr at central plane is 0 due to the assumed symmetry of the system. On the contrary, in the near interface area, the depletion of Cr cannot be ignored. The second boundary condition (BC2) indicates that, at the oxide/metal interface, the concentration of chromium is related to the initial value 28.28% or 34.5%. The interfacial

concentration of cation is studied in [26], which shows that during the later stages of oxidation, the interfacial concentration of cation increases to an almost constant value. To simplify the calculation, the ratio $\boldsymbol{\alpha}$ is considered as a constant equal to 0.413 for the parabolic oxidation law [26].

If considering the whole sample, from top surface to bottom surface, it is a problem with Dirichlet boundary conditions. However, only the top half part are presented, from the top surface down to the central plane. At the central plane, the rate of weight concentration for Cr is 0 due to symmetry. Thus, conditions given in Eq. 22 are Neumann-Dirichlet boundary conditions in our case. The Eq.20 can be solved considering the following general solution:

$$[\boldsymbol{Cr}](\boldsymbol{z},\boldsymbol{t}) = (\boldsymbol{1}-\boldsymbol{\alpha})[\boldsymbol{Cr}]_{\boldsymbol{i}}\boldsymbol{erf}(\boldsymbol{q}) + \boldsymbol{\alpha}[\boldsymbol{Cr}]_{\boldsymbol{i}} \quad (\boldsymbol{23})$$

where $[\boldsymbol{Cr}]_{\boldsymbol{i}}$ is the initial concentration of chromium; and $\boldsymbol{q} = \frac{\boldsymbol{z}}{\boldsymbol{2\sqrt{Dt}}}$. The numerical approximations of function error erf are given in [29]. By combining the numerical approximation and Eq.23, an analytical solution is obtained as:

$$[Cr](z,t) = (1-\alpha)[Cr]_i\left(1-(a_1 n + a_2 n^2 + a_3 n^3 + a_4 n^4 + a_5 n^5)e^{-q^2}\right) + \alpha[Cr]_i \quad (24)$$

with

$$\begin{cases} q = \dfrac{z}{2\sqrt{Dt}} \\ n = \dfrac{1}{1+pq} \\ p = 0.3275911, a_1 = 0.254829592, a_2 = -0.284496736, \\ a_3 = 1.421413741, a_4 = -1.453152027, a_5 = 1.061405429 \\ \alpha = 0.413 \\ |error(z)| \le 1.5E-7 \end{cases} \quad (25)$$

The chromium concentration profiles can then be calculated for the different samples conditions:

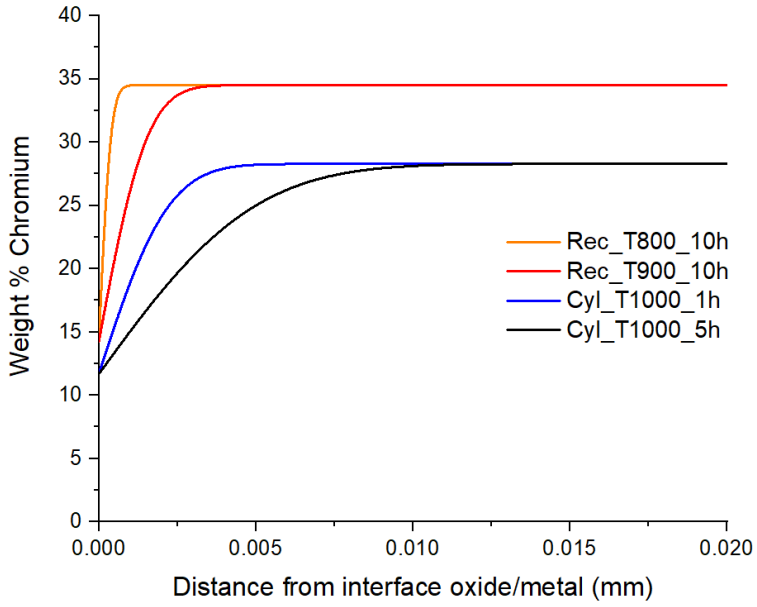


Figure 11. Chromium concentration profiles for different oxidation conditions

Fig.11 shows the chromium concentration profiles in the first 20 μm from the oxide/metal interface, which proves the chromium depletion near the interface far from the sample center where no depletion occurs, providing that the metal thickness is sufficient enough. Comparison of different oxidation conditions indicates that the depth of chromium-depleted zone increases with the time and temperature of oxidation. With longer oxidation time and higher oxidation temperature, the concentration gradient changes faster. However, it also shows that the chromium concentration equals to the initial value after 15 μm for the four samples (Table 8). Furthermore, a scanning electron microscope and Energy-dispersive X-ray spectroscopy test for chromium concentration profiles have been performed at oxidation condition of 800 °C for 1 h. It shows a variation of weight concentration of chromium within 1 μm in near interface zone, which is consistent with the present calculations. At shorter oxidation time and lower oxidation temperature, the variation of weight concentration of chromium is very difficult to detect.

Table 8. Weight concentration of chromium in the near interface zone

| Depth(μm) | 0 | 1 | 2 | 3 | 4 | 6 | 8 | 10 | 12 | 15 |
|---|---|---|---|---|---|---|---|---|---|---|
| Cyl_T1000_1h | 11.68 | 18.91 | 24.14 | 26.88 | 27.92 | 28.27 | 28.28 | 28.28 | 28.28 | 28.28 |
| Cyl_T1000_5h | 11.68 | 15.06 | 18.22 | 20.98 | 23.25 | 26.25 | 27.63 | 28.11 | 28.25 | 28.28 |
| Rec_T800_10h | 14.25 | 34.45 | 34.5 | 34.5 | 34.5 | 34.5 | 34.5 | 34.5 | 34.5 | 34.5 |
| Rec_T900_10h | 14.25 | 26.2 | 32.45 | 34.23 | 34.48 | 34.5 | 34.5 | 34.5 | 34.5 | 34.5 |

6.3 Investigation on chemical/diffusion strain and diffusion stress

Due to the important variation of chromium concentration in the near-surface zone, we propose to associate a strain gradient related to the chromium concentration profiles [30].

$$\acute{\boldsymbol{\varepsilon}}^{\boldsymbol{diffusion}}(\boldsymbol{z}) = \boldsymbol{\eta}([\boldsymbol{Cr}](\boldsymbol{z},\boldsymbol{t}) - [\boldsymbol{Cr}]_{\boldsymbol{i}})\acute{\boldsymbol{I}} \quad (\mathbf{26})$$

where $\acute{\boldsymbol{\varepsilon}}^{\boldsymbol{diffusion}}(\boldsymbol{z})$ is the strain caused by diffusion, which is a function of z; $\boldsymbol{\eta}$ is a constant coefficient coupling the chromium concentration profiles to the diffusion strain; $[\boldsymbol{Cr}](\boldsymbol{z},\boldsymbol{t})$ is chromium concentration profiles as a function of z; $[\boldsymbol{Cr}]_{\boldsymbol{i}}$ is the initial concentration of chromium.

The relation between the stress and the elastic stain is given by Hooke's model (Eq.10), which can also be written as, with Lamé's coefficients , μ :

$$\acute{\boldsymbol{\sigma}} = \boldsymbol{\lambda trace}\left(\acute{\boldsymbol{\varepsilon}}^{\boldsymbol{elastic}}\right)\acute{\boldsymbol{I}} + \mathbf{2}\mu\acute{\boldsymbol{\varepsilon}}^{\boldsymbol{elastic}} \quad (\mathbf{27})$$

The stress tensor $\acute{\boldsymbol{\sigma}}$ (Eq.11) and elastic strain tensor $\acute{\boldsymbol{\varepsilon}}^{\boldsymbol{elastic}}$ are considered as in-plane isotropic:

$$\acute{\boldsymbol{\sigma}} = \begin{pmatrix} \boldsymbol{\sigma} & \mathbf{0} & \mathbf{0} \\ \mathbf{0} & \boldsymbol{\sigma} & \mathbf{0} \\ \mathbf{0} & \mathbf{0} & \boldsymbol{\sigma_N} \end{pmatrix} \boldsymbol{and}\ \acute{\boldsymbol{\varepsilon}}^{\boldsymbol{elastic}} = \begin{pmatrix} \boldsymbol{\varepsilon}^{\boldsymbol{elastic}} & \mathbf{0} & \mathbf{0} \\ \mathbf{0} & \boldsymbol{\varepsilon}^{\boldsymbol{elastic}} & \mathbf{0} \\ \mathbf{0} & \mathbf{0} & \boldsymbol{\varepsilon}^{\boldsymbol{elastic}}{}_{\boldsymbol{N}} \end{pmatrix} \quad (\mathbf{28})$$

A proportional relationship between in-plane stress $\boldsymbol{\sigma}$ and normal stress $\boldsymbol{\sigma_N}$ in the metal is assumed:

$$\boldsymbol{\sigma_N} = \boldsymbol{\beta\sigma} \quad (\mathbf{29})$$

As proposed in Eq.18 from experimental observations, $\boldsymbol{\beta}$ = 1. By combining Eq.27, Eq.28 and Eq.29, the relation between elastic strain $\boldsymbol{\varepsilon^{elastic}}$ and normal elastic strain $\boldsymbol{\varepsilon^{elastic}}_{\boldsymbol{N}}$ in the metal is obtained:

$$\boldsymbol{\varepsilon^{elastic}}_{\boldsymbol{N}} = \frac{\boldsymbol{\beta - 2\nu_m}}{\boldsymbol{1 - \nu_m - \beta\nu_m}} \boldsymbol{\varepsilon^{elastic}} \quad (\mathbf{30})$$

The in-plane stress $\boldsymbol{\sigma}$ in metal can then be calculated:

$$\boldsymbol{\sigma} = \frac{\boldsymbol{E_m}}{\boldsymbol{1 - \nu_m - \beta\nu_m}} \boldsymbol{\varepsilon^{elastic}} \quad (\mathbf{31})$$

As presented in Eq.16, the strain in metal layer includes different components. After modifying it by adding $\boldsymbol{\varepsilon^{diffusion}}$, the strain in metal layer is:

$$\boldsymbol{\varepsilon^{total}} = \boldsymbol{\varepsilon^{elastic}} + \boldsymbol{\varepsilon^{viscoplastic}} + \boldsymbol{\varepsilon^{thermal}} + \boldsymbol{\varepsilon^{diffusion}} \quad (\mathbf{32})$$

Eq.31 can be expressed as:

$$\boldsymbol{\sigma} = \frac{\boldsymbol{E_m}}{\boldsymbol{1 - \nu_m - \beta\nu_m}} \left(\boldsymbol{\varepsilon^{total}} - \boldsymbol{\varepsilon^{viscoplastic}} - \boldsymbol{\varepsilon^{thermal}} - \boldsymbol{\varepsilon^{diffusion}}\right) \quad (\mathbf{33})$$

Eq. 33 can be split into 2 terms: the diffusion stress and another term:

$$\boldsymbol{\sigma^{diffusion}} = \frac{\boldsymbol{-E_m}}{\boldsymbol{1 - \nu_m - \beta\nu_m}} \boldsymbol{\varepsilon^{diffusion}} \quad (\mathbf{34})$$

$$\boldsymbol{\sigma^{else}} = \frac{\boldsymbol{E_m}}{\boldsymbol{1 - \nu_m - \beta\nu_m}} \left(\boldsymbol{\varepsilon^{total}} - \boldsymbol{\varepsilon^{viscoplastic}} - \boldsymbol{\varepsilon^{thermal}}\right) \quad (\mathbf{35})$$

Because $\boldsymbol{\varepsilon^{diffusion}}$ is related to chromium concentration profiles varying with depth z, $\boldsymbol{\sigma^{diffusion}}$ is a function of z. To find coefficient $\boldsymbol{\eta}$, the boundary value of stress is considered, which can be related to the experimental results. For metal layer, when z=0,

$$\boldsymbol{\sigma(0) = \sigma^{diffusion}(0) + \sigma^{else} \Leftrightarrow \sigma^{else} = \sigma(0) - \sigma^{diffusion}(0)} \quad (\mathbf{36})$$

We assume that $\boldsymbol{\sigma^{else}}$does not depend on z. By combining Eq.19, Eq.26, Eq.34 and Eq.36, the equation of mechanical balance becomes:

$$\int_{\boldsymbol{0}}^{\boldsymbol{h_m/2}} \left(\boldsymbol{\sigma(0)} + \frac{\boldsymbol{E_m}}{\boldsymbol{1 - \nu_m - \beta\nu_m}} \boldsymbol{\eta}([\boldsymbol{Cr}](\boldsymbol{0,t}) - [\boldsymbol{Cr}]_{\boldsymbol{i}}) - \frac{\boldsymbol{E_m}}{\boldsymbol{1 - \nu_m - \beta\nu_m}} \boldsymbol{\eta}([\boldsymbol{Cr}](\boldsymbol{z,t}) - [\boldsymbol{Cr}]_{\boldsymbol{i}})\right) \boldsymbol{dz} + \int_{\boldsymbol{-h_{ox}}}^{\boldsymbol{0}} \boldsymbol{\sigma_{ox}}\, \boldsymbol{dz} = \boldsymbol{0} \quad (\mathbf{37})$$

where $[\boldsymbol{Cr}](\boldsymbol{0,t})$ is the concentration of chromium at the oxide/metal interface. To obtain the value of $\boldsymbol{\eta}$, the unknown value of $\boldsymbol{\sigma_{ox}}$in Eq.37 is required, which can be found in [31]. However, the $\boldsymbol{\sigma_{ox}}$ in [31] is studied under oxidation temperature. On the contrary, the $\boldsymbol{\sigma_{ox}}$ in Eq.37 should be the results at room temperature, which can be calculated by adding the thermal stress component, but neglecting the relaxation phenomena:

$$\boldsymbol{\sigma_{ox} = \sigma_{ox}^{T_{oxidation}} - \frac{E_{ox}}{1-\nu_{ox}}(\alpha_{ox} - \alpha_{met})(T_{room} - T_{oxidation})} \quad (38)$$

with thermal expansion coefficient of oxide layer $\boldsymbol{\alpha_{ox}}$, which is 5.67E-6 $K^{-1}$ [32]; thermal expansion coefficient of metal layer $\boldsymbol{\alpha_{met}}$, which is 12.93E-6 $K^{-1}$ [32]; room temperature $\boldsymbol{T_{room}}$ is 298 K and oxidation temperature $\boldsymbol{T_{oxidation}}$ that depends on the sample conditions. The other used parameters for the different samples are presented in Table 9:

Table 9: Input data and related parameters in Eq.37 and Eq.38 [31, 33]

| | $E_m$ (MPa) | $\nu_m$ | $\frac{h_m}{2}$ (mm) | $\sigma(0)$ (MPa) | $E_{ox}$ (MPa) | $\nu_{ox}$ | $h_{ox}$ (mm) | $\sigma_{ox}^{T_{oxidation}}$ (MPa) |
|---|---|---|---|---|---|---|---|---|
| Cyl_T1000_1h | 160000 | 0.3 | 0.45 | -588.09 | 299700 | 0.270 | 0.00097 | -144.1±18.5 |
| Cyl_T1000_5h | 160000 | 0.3 | 0.45 | -1178.70 | 299700 | 0.270 | 0.00216 | -133.1±23.9 |
| Rec_T800_10h | 170000 | 0.3 | 0.2 | -556.68 | 301100 | 0.273 | 0.0006 | -277.8±11.4 |
| Rec_T900_10h | 165000 | 0.3 | 0.2 | -969.93 | 300400 | 0.271 | 0.00101 | -150.0±34.3 |

Because of the different oxidation temperatures, the values of $\boldsymbol{E_m}$, $\boldsymbol{E_{ox}}$ and $\boldsymbol{\nu_{ox}}$ are different. The residual stresses at room temperature can be calculated by using Eq.38 and the parameters in Table 9, which can also be measured by Raman spectroscopy [34] or XRD [11]. The comparison of these results with our calculations is shown in Table 10.

Table 10: Comparison of residual stresses at room temperature

| Calculated results | | Measured results for system Ni30Cr/Cr2O3 [11, 34] | | | |
|---|---|---|---|---|---|
| Sample | $\sigma_{ox}$ (GPa) | Sample | $\sigma_{ox}$ (GPa) | Sample | $\sigma_{ox}$ (GPa) |
| Cyl_T1000_1h | -3.05 | 1000°C_3h | -2.60, -2.35, -3.05 | | |
| Cyl_T1000_5h | -3.04 | | | 1000°C_18h | -3.00 |
| Rec_T800_10h | -2.61 | 800°C_3h | -1.56 | 800°C_18h | -1.84 |
| Rec_T900_10h | -2.77 | 900°C_3h | -1.94 | 900°C_18h | -2.40, -2.10, -2.50 |

Table 10 shows that the calculated values of residual stresses at room temperature are smaller than the measured values, but the oxidation time are different. However, they are at the same order of magnitude. The calculated results are chosen for the subsequent calculations.

As proposed in Eq.18, $\boldsymbol{\beta}$ = 1 and in Eq.26, $\boldsymbol{\eta}$ is a constant coefficient. Eq.37 can be transformed into:

$$\boldsymbol{\eta = \frac{-\int_{-h_{ox}}^{0} \sigma_{ox}\, dz - \int_{0}^{h_m/2} \sigma(0) dz}{\int_{0}^{h_m/2} \frac{E_m}{1-2\nu_m}\left([Cr](0,t) - [Cr](z,t)\right) dz}} \quad (38)$$

The coefficient $\boldsymbol{\eta}$ coupling diffusion with strain is calculated:

Table 11. Values for the coefficient $\boldsymbol{\eta}$

| Code name | coefficient $\boldsymbol{\eta}$ |
|---|---|
| Cyl_T1000_1h | -8.98E-03 |
| Cyl_T1000_5h | -1.80E-02 |
| Rec_T800_10h | -6.57E-03 |
| Rec_T900_10h | -1.18E-02 |

$\boldsymbol{\eta}$ is strongly related to $\boldsymbol{\sigma_{ox}}$ and $\boldsymbol{\sigma(0)}$. Table 11 shows that the order of magnitudes of coefficient $\boldsymbol{\eta}$ is around -1E-02, from which the diffusion stress for four samples can in return be calculated.

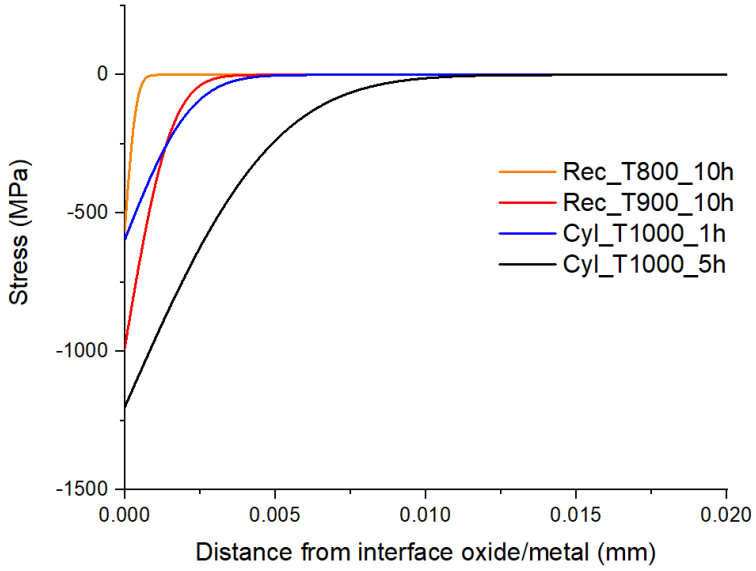


Figure 12 Diffusion stress calculated for the four samples

As shown in Fig.12, the diffusion stress calculated for the four samples in the first 20 μm from the oxide/metal interface is plotted, which gives a maximum diffusion stress of -1200 MPa for sample Cyl_T1000_5h. The important variation of chromium depletion leads to a diffusion stress with maximum magnitudes between -500 and -1500 MPa. Such a stress cannot be ignored.

Therefore, to observe the effect of adding diffusion stress in the modelling, several results are plotted in the same figure, which includes : the stress without the diffusion stress (corresponding to modelling that can be found in [12, 25]), the stress in the metal layer with the diffusion stress (using the models including the term calculated with Eq. 34 using the values of $\boldsymbol{\eta}$ in Table 11) and the experimental results presented in Figs 6-9.

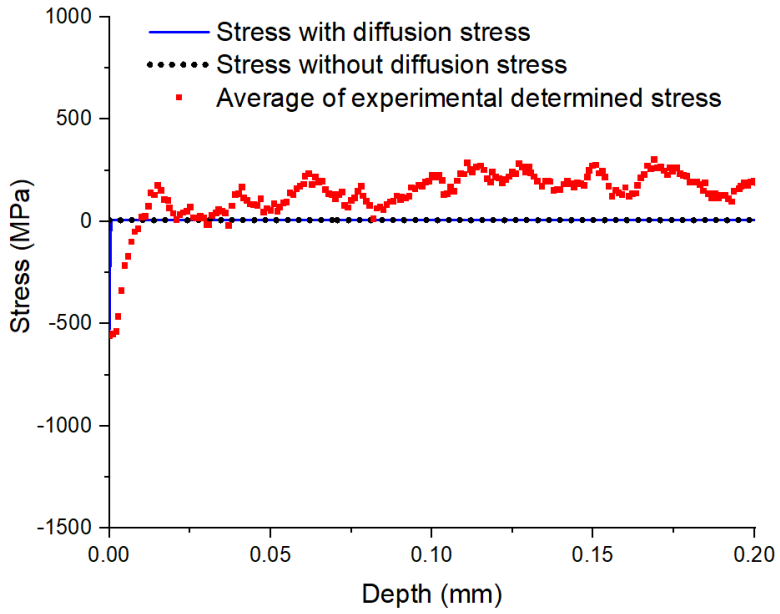


Figure 13.a Stress distribution in sample Rec_T800_10h

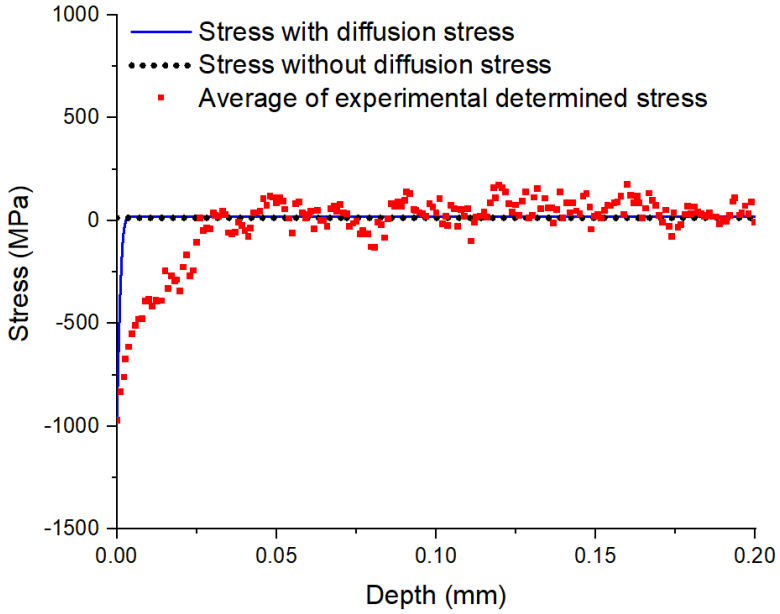


Figure 13.b Stress distribution in sample Rec_T900_10h

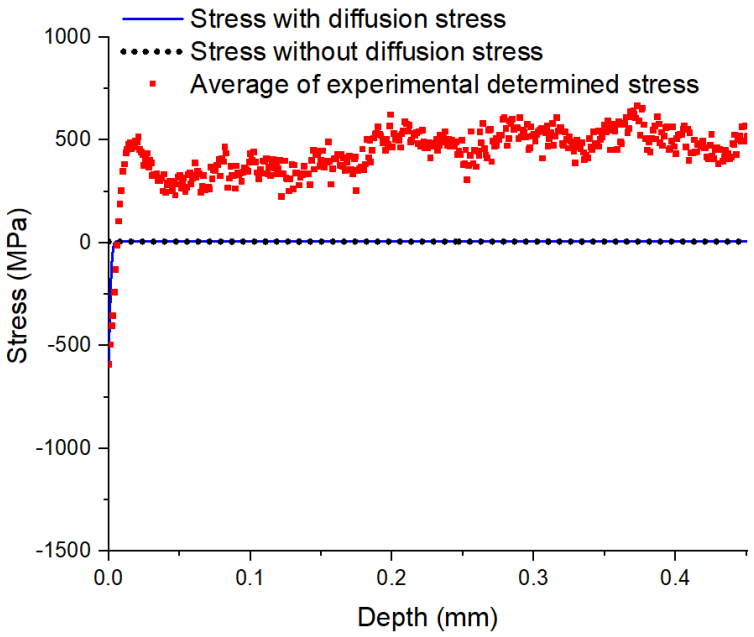


Figure 13.c Stress distribution in sample Cyl_T1000_1h

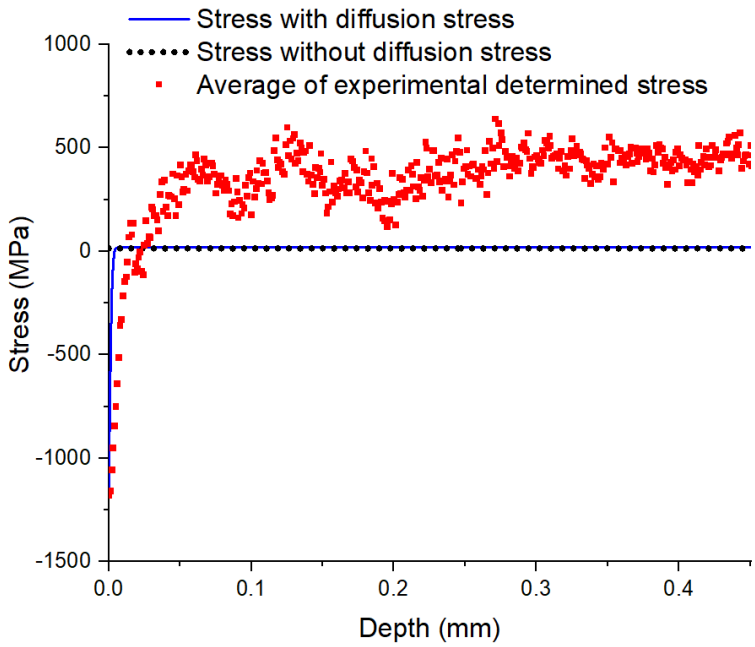


Figure 13.d Stress distribution in sample Cyl_T1000_5h

The results of Fig.13.a-d are compared in Table 12.

Table 12. Comparison of the four samples

| | Experimental results | | With diffusion stress | | Without diffusion stress |
|---|---|---|---|---|---|
| | Depth for 0 MPa | Average stress after depth for 0 MPa | Depth for 0 MPa | Average stress after depth for 0 MPa | Average stress |
| Cyl_T1000_1h | 7 μm | 452.3 MPa | 4 μm | 8.4 MPa | 6.6 MPa |
| Cyl_T1000_5h | 14 μm | 388.8 MPa | 4 μm | 18.3 MPa | 14.6 MPa |
| Rec_T800_10h | 10 μm | 151.5 MPa | 1 μm | 8.52 MPa | 7.8 MPa |
| Rec_T900_10h | 26 μm | 41.7 MPa | 3 μm | 18.60 MPa | 14.0 MPa |

Fig.12.a-d show that the stress in metal far from the interface zone is a positive value for the model with and without the diffusion stress. After adding the diffusion stress, a stress gradient is systematically predicted for the near interface zone.

For sample Cyl_T1000_1h and Cyl_T1000_5h, the stress gradient in the near interface zone with diffusion stress is very similar to the experimental results. The gradient depths have also the same order of magnitude. However, the average stress after depth of 0 MPa of experimental results is different from the results with (or without) diffusion stress. By comparing these two samples, it shows that with a longer oxidation time, the stress should be lower in the bulk metal, whereas the predicted model values are opposite (with or without diffusion stress). This can be related to the stress-free values of characteristic diffraction pattern ($\boldsymbol{2\theta_0}$) or the experimental uncertainties that are quite important in the metal as well as the standard deviation that corresponds to the effect of different rotations on each sample.

For sample Rec_T800_10h and Rec_T900_10h, the stress gradient in the near interface zone is present for all the simulations with diffusion stress, but the gradient depths are ten times smaller than the experimental ones. Nevertheless, the average stress after depth of 0MPa is more consistent to the experimental results especially for Rec_T900_10h (see Figure 13.b). The same reason as previously can be invoked to explain the differences. This may also be caused by the thinner thickness of metal layer or the specific shape of samples, which requires further investigations.

## 7. Conclusion

The present work is based on the stress-depth evolution that was obtained by treating the results of synchrotron in transmission mode measurements obtained in-situ at room temperature at DESY. To investigate the residual stress distribution in the metallic substrate after oxidation, a $\sin^2\boldsymbol{\varphi}$ method, variant of $\sin^2\boldsymbol{\psi}$ method, is developed.

Firstly, a normal stress $\boldsymbol{\sigma_N}$ and a stress gradient as a function of depth in substrate are evidenced. The overlap clearly indicates that the stress $\boldsymbol{\sigma}$ and $\boldsymbol{\sigma_N}$ are identical in the metal. As the thickness of the samples is hundred times thicker than the thickness of the oxidation layer oxidation, the existence of normal stress $\boldsymbol{\sigma_N}$ in the metal is very reasonable.

Secondly, the largest part of the stresses distribution is ranged from 0 MPa to 500 MPa and presents a gradient distribution, which is located in the near interface zone (up to 15μm before roughly constant values). The stress varies towards the surface in a non-linear way. With a lower oxidation temperature

or lower oxidation time, the absolute stress at the oxide/metal interface is smaller and the depth of stress gradient is thinner.

Moreover, we proposed adding the diffusion stress in existing thermomechanical model to explain the stress gradient in the near interface zone. Due to the rapid variation of chromium depletion in the near-surface zone, the diffusion stress changes as a function of z. After adding this diffusion stress, the stress distribution accords better with the average of measured stress compared to the modeling without diffusion stress. However, the correspondence of the gradient stress distribution between experiments and modelling requires further improvement. Numerical values for the coupling of chromium concentration with diffusion/chemical stress have been obtained. These values strongly influence the level of calculated stress that may add uncertainty on the obtained calculations.

The present study fills a gap in the literature by using high-energy X-ray in transmission mode to measure the stress distribution in depth metal layer and by proposing a model to calculate the stress distribution for comparison. From an experimental point of view, the oxidation conditions, even the shape of samples can influence the stress distribution. From a modelling point of view, the input parameters and the different mechanisms can influence the results. The comparison is thus difficult because of the numerous uncertainties and errors origins. However, the observation of gradient and its prediction, by adding the diffusion stress component in the thermomechanical modeling, leads to a better explanation of part of the stress distribution in the metal layer.

This study aims to contribute to this growing area of research by exploring the local stress distribution in the substrate, which helps us to understand better the mechanism behind and to prevent the damage caused by residual stress. It also provides a new point of view to further evaluate the effect of surface treatment and surface modification, for example, by analyzing the stress distribution in metal layer to evaluate the effect of doping reactive elements on the surface.

Acknowledgments: The authors gratefully acknowledge the Deutsches Elektronen-Synchrotron (DESY-Petra III, Hamburg, Germany) for provision of beamtime at the PETRA P07-EH2 beamline.

References

[1] M. Schütze, Protective Oxide Scales and Their Breakdown, NJ, 1991.
[2] P. Kofstadt, High Temperature Corrosion, London, 1998.
[3] A.M. Huntz, B. Pieraggi, Oxydation des matériaux métalliques, Hermès Science, Paris, 2003.
[4] B. Panicaud, J.-L. Grosseau-Poussard, Z. Tao, F. Rakotovao, G. Geandier, P.-O. Renault, P. Goudeau, N. Boudet, N. Blanc, Frequency analysis for investigation of the thermomechanical mechanisms in thermal oxides growing on metals, Acta Mech. 228 (2017) 3595–3617. https://doi.org/10.1007/s00707-017-1899-z.
[5] Z.J. Tao, F. Rakotovao, J.L. Grosseau-Poussard, B. Panicaud, Determination of Stress Fields and Identification of Thermomechanical Parameters in a Thermally Grown Oxide under Thermal Cycling Loadings, Using Advanced Models, AMR. 996 (2014) 896–901. https://doi.org/10.4028/www.scientific.net/AMR.996.896.
[6] Z. Wang, J.-L. Grosseau-Poussard, B. Panicaud, G. Geandier, P.-O. Renault, P. Goudeau, N. Boudet, N. Blanc, F. Rakotovao, Z. Tao, Viscoplasticity and growth strain parameters identification by full modelling optimization during the high temperature oxidation of Ni28Cr modified by the reactive element yttria or zirconium, Computational Materials Science. 180 (2020) 109689. https://doi.org/10.1016/j.commatsci.2020.109689.

[7] A.M. Huntz, J.G. Zhao, Deteriiiination of the Oxidation Stress Distribution in a Duplex Oxide-Metallic Substrate System by a Curvature Method, (n.d.) 7.
[8] M. Parise, O. Sicardy, G. Cailletaud, Modelling of the mechanical behavior of the metal–oxide system during Zr alloy oxidation, Journal of Nuclear Materials. 256 (1998) 35–46. https://doi.org/10.1016/S0022-3115(98)00045-2.
[9] C. Li, S.D.M. Jacques, Y. Chen, P. Xiao, A.M. Beale, M. di Michiel, N. Markossan, P. Nylen, R.J. Cernik, Precise strain profile measurement as a function of depth in thermal barrier coatings using high energy synchrotron X-rays, Scripta Materialia. 113 (2016) 122–126. https://doi.org/10.1016/j.scriptamat.2015.10.032.
[10] B. Panicaud, J.-L. Grosseau-Poussard, M. Kemdehoundja, J.-F. Dinhut, Mechanical features optimization for oxide films growing on alloy, Computational Materials Science. 46 (2009) 42–48. https://doi.org/10.1016/j.commatsci.2009.02.003.
[11] M. Guerain, Contribution à l'étude des mécanismes de relaxation de contraintes dans les films de chromine formés sur Ni-30Cr et Fe-47Cr : approche multi-échelle par spectroscopie Raman et microdiffraction Synchrotron, PhD Thesis, Université de La Rochelle, La Rochelle, France, 2012.
[12] Z. Wang, J.-L. Grosseau-Poussard, B. Panicaud, G. Geandier, P.-O. Renault, P. Goudeau, N. Boudet, N. Blanc, F. Rakotovao, Z. Tao, Determination of Residual Stresses in an Oxidized Metallic Alloy under Thermal Loadings, Metals. 8 (2018) 913. https://doi.org/10.3390/met8110913.
[13] W. Przybilla, M. Schutze, Role of Growth Stresses on the Structure of Oxide Scales on Nickel at 800 and 900°C, (n.d.) 43.
[14] C. Liu, A.-M. Huntz, J.-L. Lebrun, Origin and development of residual stresses in the Ni◎NiO system: in-situ studies at high temperature by X-ray diffraction, Materials Science and Engineering: A. 160 (1993) 113–126. https://doi.org/10.1016/0921-5093(93)90504-8.
[15] J.G. Goedjen, J.H. Stout, Q. Guo, D.A. Shores, Evaluation of stresses in Ni◎NiO and Cr◎Cr2O3 during high temperature oxidation by in situ X-ray diffraction, Materials Science and https://doi.org/10.1016/0921-5093(94)90483-9.
[16] L. Le, D.W. Ming, B. Sutter, 2015. Transmission x-ray diffraction (xrd) patterns relevant to the msl chemin 2.
[17] R. Delhez, S.J. Van der Gaast, A. Wielders, J.L. de Boer, R.B. Helmholdt, J. van Mechelen, C. Reiss, L. Woning, H. Schenk, Tandem transmission/reflection mode XRD instrument including XRF for in situ measurement of Martian rocks and soils, in: R.B. Hoover, A.Y. Rozanov, R.R. Paepe (Eds.), Waikoloa, Hawai'i, United States, 2003: p. 87. https://doi.org/10.1117/12.457340.
[18] B.B. He, U. Preckwinkel, K.L. Smith, 2003. Comparison between conventional and two-dimensional xrd 46, 6.
[19] J. Kieffer, V. Valls, N. Blanc, C. Henning, New tools calibrating diffraction setups', Journal of synchrotron radiation 27 (2020) 558-566.
[20] F.A. Fernandes, T.L. Christiansen, G. Winther, M.A. Somers, On the determination of stress profiles in expanded austenite by grazing incidence X-ray diffraction and successive layer removal, Acta Materialia 94 (2015) 271–280.
[21] M. Marciszko, A. Baczmański, C. Braham, M. Wróbel, W. Seiler, S. Wroński, K. Berent, Analysis of stresses and crystal structure in the surface layer of hexagonal polycrystalline materials: a new methodology based on grazing incidence diffraction, Journal of Applied Crystallography 49 (2016) 85-102.
[22] D. Apel, M. Klaus, M. Genzel, C. Genzel, Rietveld-based energy-dispersive residual stress evaluation: analysis of complex stress fields sigma_ij(z), Journal of Applied Crystallography 47 (2014) 511-526.

[23] C. Genzel, M. Meixner, D. Apel, M. Boin, M. Klaus, Nondestructive residual stress depth profile analysis at the inner surface of small boreholes using energy-dispersive diffraction under laboratory conditions, Journal of Applied Crystallography 54 (2021).
[24] S. Petrovic, N. Bundaleski, M. Radovic, Z. Ristic, G. Gligoric, D. Perusko, S. Zec, Structure and surface composition of NiCr sputtered thin films, Sci Sintering. 38 (2006) 155–160. https://doi.org/10.2298/SOS0602155P.
[25] B. Panicaud, Contraintes « de croissance » et cinétiques d'oxydation dans des couches d'oxydes thermiques de Fer et de Nickel ; Etude in-situ par Diffraction des Rayons X et modélisation, PhD Thesis, Université de La Rochelle, La Rochelle, France, 2004.
[26] D.P Whittle, D.J Evans, D.B Scully, G.C Wood, Compositional changes in the underlying alloy during the protective oxidation of alloys, Acta Metallurgica, Volume 15, Issue 9, 1967, Pages 1421-1430, https://doi.org/10.1016/0001-6160(67)90173-3.
[27] J. Růžičková, B. Million, Self-diffusion of the components in the F.C.C. phase of binary solid solutions of the Fe-Ni-Cr system, Materials Science and Engineering. 50 (1981) 59–64. https://doi.org/10.1016/0025-5416(81)90086-0.
[28] K. Monma, H. Suto, H. Oikawa. J. Jpn, inst, Met, 28(1964) 188-192.
[29] A. Milton, S. Irene, Abramowitz and Stegun, U.S., 1964.
[30] D.Fettre, Aspects mécaniques de l'oxydation haute température du zirconium: modélisation des champs de contrainte et suivi expérimental multi technique des endommagements, PhD Thesis, Université de Compiègne, Compiègne, France, 2017.
[31] Z.J. Tao, Etude expérimentale et modélisation des caractéristiques mécaniques d'une couche d'oxyde sous charges thermiques. PhD thesis, Université de Technologie de Troyes, Troyes, 2018.
[32] S. Daghigh, Evolution des contraintes dans le système Ni70Cr30/Cr2O3 en fonction de la température. Etude in situ par diffraction des rayons X et modélisation = Evolution of stresses in Ni70Cr30/Cr2O3 system as a function of the temperature. In situ experiments with. PhD thesis, Paris XI Orsay University 1996.
[33] Y. Wang, H. Fang, C.L. Zacherl, Z. Mei, S. Shang, L.-Q. Chen, P.D. Jablonski, Z.-K. Liu, First-principles lattice dynamics, thermodynamics, and elasticity of Cr2O3, Surface Science. 606 (2012) 1422–1425. https://doi.org/10.1016/j.susc.2012.05.006.
[34] F.N. Rakotovao, Relaxation des contraintes dans les couches de chromine développées sur alliages modèles (NiCr et Fe47Cr). Apport de la diffraction in situ à haute température sur rayonnement Synchrotron à l'étude du comportement viscoplastique. Effets d'éléments réactifs, PhD thesis, Université de La Rochelle, 2016.